Article

Cell

Unleashing Type-2 Dendritic Cells to Drive Protective Antitumor CD4$^+$ T Cell Immunity

Graphical Abstract

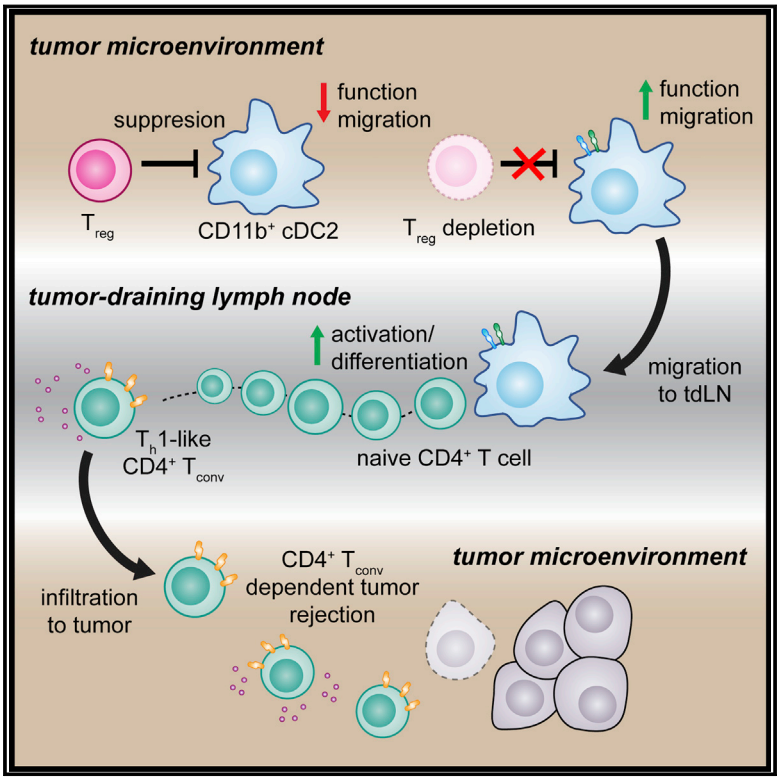

Authors

Mikhail Binnewies, Adriana M. Mujal, Joshua L. Pollack, ..., Chun J. Ye, Edward W. Roberts, Matthew F. Krummel

Correspondence

matthew.krummel@ucsf.edu

In Brief

A subtype of conventional dendritic cells, cDC2, are able to prime CD4$^+$ T cells for antitumor functions and the presence of cDC2 in human cancer samples may serve as a predictive biomarker for survival and response to immune checkpoint blockade.

Highlights

- cDC2 initiate activation but not differentiation of antitumor CD4$^+$ T_{conv}
- T_{reg} depletion relieves cDC2 suppression driving antitumor CD4$^+$ T_{conv} differentiation
- Human equivalent of mouse cDC2 are present in the tumor and draining lymph node
- The balance of human cDC2/T_{reg} in the TME dictates T cell quality and prognosis

Data Resources

GSE125680

Binnewies et al., 2019, Cell *177*, 556–571
April 18, 2019
https://doi.org/10.1016/j.cell.2019.02.005

CellPress

Cell

Article

Unleashing Type-2 Dendritic Cells to Drive Protective Antitumor CD4$^+$ T Cell Immunity

Mikhail Binnewies,[1,7,9] Adriana M. Mujal,[1,8,9] Joshua L. Pollack,[6] Alexis J. Combes,[1,2] Emily A. Hardison,[1] Kevin C. Barry,[1,2] Jessica Tsui,[1,2] Megan K. Ruhland,[1] Kelly Kersten,[1] Marwan A. Abushawish,[6] Marko Spasic,[3] Jonathan P. Giurintano,[4] Vincent Chan,[1,2] Adil I. Daud,[3] Patrick Ha,[4] Chun J. Ye,[5] Edward W. Roberts,[1] and Matthew F. Krummel[1,2,10,*]

[1]Department of Pathology, University of California, San Francisco, San Francisco, CA 94143, USA
[2]UCSF Immunoprofiler Initiative, University of California, San Francisco, San Francisco, CA 94143, USA
[3]Department of Medicine, University of California, San Francisco, San Francisco, CA 94143, USA
[4]Department of Otolaryngology-Head and Neck Surgery, University of California, San Francisco, San Francisco, CA 94143, USA
[5]Institute of Human Genetics, University of California, San Francisco, San Francisco, CA 94143, USA
[6]Pionyr Immunotherapeutics, San Francisco, CA 94080, USA
[7]Present address: Pionyr Immunotherapeutics, San Francisco, CA 94080, USA
[8]Present address: Immunology Program, Memorial Sloan Kettering Cancer Center, New York, NY 10065, USA
[9]These authors contributed equally
[10]Lead Contact
*Correspondence: matthew.krummel@ucsf.edu
https://doi.org/10.1016/j.cell.2019.02.005

SUMMARY

Differentiation of proinflammatory CD4$^+$ conventional T cells (T_{conv}) is critical for productive antitumor responses yet their elicitation remains poorly understood. We comprehensively characterized myeloid cells in tumor draining lymph nodes (tdLN) of mice and identified two subsets of conventional type-2 dendritic cells (cDC2) that traffic from tumor to tdLN and present tumor-derived antigens to CD4$^+$ T_{conv}, but then fail to support antitumor CD4$^+$ T_{conv} differentiation. Regulatory T cell (T_{reg}) depletion enhanced their capacity to elicit strong CD4$^+$ T_{conv} responses and ensuing antitumor protection. Analogous cDC2 populations were identified in patients, and as in mice, their abundance relative to T_{reg} predicts protective ICOS$^+$ PD-1^{lo} CD4$^+$ T_{conv} phenotypes and survival. Further, in melanoma patients with low T_{reg} abundance, intratumoral cDC2 density alone correlates with abundant CD4$^+$ T_{conv} and with responsiveness to anti-PD-1 therapy. Together, this highlights a pathway that restrains cDC2 and whose reversal enhances CD4$^+$ T_{conv} abundance and controls tumor growth.

INTRODUCTION

Recent therapeutic advances blocking T cell checkpoint molecules like CTLA-4 or PD-1/PD-L1 have demonstrated clinical success, but in only a subset of patients (Hodi et al., 2008; Topalian et al., 2014). Limitations in efficacy can be attributed to tumor-induced generation of dysfunctional and exhausted T cells reminiscent of exhaustion seen in chronic infection (Schietinger et al., 2016). Irreversibly exhausted T cells in the tumor microenvironment (TME) are unlikely to be rescued by immune checkpoint blockades (ICB) (Pauken et al., 2016; Philip et al., 2017). Thus, in patients with poor T cell infiltration or exhaustion, improving priming may be necessary to engage effective antitumor immunity (Philip et al., 2017).

While CD8$^+$ T cells are often immunotherapeutic targets due to their role in tumor cell cytolysis, CD4$^+$ T_{conv} are emerging as an important contributor to antitumor responses. Effector CD4$^+$ T_{conv} can augment immunity by licensing dendritic cells (DC) (Behrens et al., 2004) and stimulating pro-inflammatory myeloid cell programs (Corthay et al., 2005). Notably, effective anti-CTLA-4 therapy generates ICOS$^+$PD-1^{lo} CD4$^+$ T helper 1-like (T_h1-like) effector CD4$^+$ T_{conv} critical for an antitumor response (Fan et al., 2014). Conversely, presence of PD-1^{hi} CD4$^+$ T_{conv} cells, correlated with high tumor burden and likely T cell exhaustion, is a negative prognostic indicator for ICB (Zappasodi et al., 2018). As such, the processes contributing to antitumor CD4$^+$ T_{conv} activation and differentiation merit further investigation.

Prior to tumor infiltration, antitumor T cells are activated in the tumor-draining lymph node (tdLN) by antigen-presenting cells (APC) such as conventional dendritic cells (cDC) that present antigen and provide co-stimulation and cytokines to tumor antigen-specific T cells. There has long been interest to augment cDC as a means to boost T cell effector function, but approaches like vaccination or administration of cDC growth factors are susceptible to endogenous immunosuppressive cells such as T_{reg} that can potently suppress cDC (Bauer et al., 2014). The diversity of cDC populations, however, makes it unclear if specific subsets are selectively impacted.

cDC can be divided into cDC1 and cDC2 populations that are either LN resident or migrate to the LN from peripheral tissues (Merad et al., 2013). cDC1 and cDC2 can take on specialized roles in CD8$^+$ and CD4$^+$ T cell priming by differentially processing and presenting antigen (Gutiérrez-Martínez et al., 2015) and producing cytokines (Merad et al., 2013). cDC1 are critical for directing CD8$^+$ T cell immunity to various pathogens (Bedoui et al., 2009) and

antitumor responses (Broz et al., 2014; Roberts et al., 2016; Salmon et al., 2016), while cDC2, a heterogeneous population, preferentially initiate $CD4^+$ T_{conv} responses in several conditions (Gao et al., 2013; Krishnaswamy et al., 2017). While the division of labor between cDC1 and cDC2 in engaging $CD8^+$ and $CD4^+$ T cells, respectively, is well established, tissue type and the nature of the challenge may determine whether they tolerize or activate their T cell partners. Indeed, the specific cDC roles in eliciting anti-tumor $CD4^+$ T_{conv} immunity remain unresolved.

We applied single-cell RNA-sequencing (scRNA-seq) to myeloid populations from tdLNs in mouse and human to understand the diversity and function of cell types and how the variance in TME might affect the nature of the $CD4^+$ T_{conv} generated. We then sought to understand how therapeutic intervention altered the outcome of $CD4^+$ T_{conv} priming. We confirmed these findings in humans determining how $CD4^+$ T_{conv} phenotype and cDC composition are connected.

RESULTS

Myeloid Heterogeneity at Single-Cell Resolution

To define the myeloid populations capable of antitumor $CD4^+$ T_{conv} priming, we sorted B16-F10 tdLN myeloid cells ($CD90.2^-$ $B220^-$ $NK1.1^-$ and $CD11c^+$ or $CD11b^+$) and performed scRNA-seq using the 10X Genomics Chromium platform paired with deep sequencing. Analysis of 4133 tdLN myeloid cells yielded 10 unique population clusters (Figures 1A and S1A).

To determine cluster identity, we generated gene signatures of populations expected in the LN from publically available data (Heng and Painter, 2008) and plotted expression of these on the tdLN *t*-SNE plot (Figure 1B; Table S1). Clusters 8 and 9 appeared to be lymphocyte contaminants and were subsequently excluded (data not shown). We then overlaid canonical myeloid markers to explore the cluster identities. *Ccr7* and *Itgax* demarcated migratory (clusters 0, 1, 2, 4, and 6) and resident (clusters 3, 5, and 7) DCs, consistent with our assignments (Figure S1B). cDC clusters (0–4, 6–7) were confirmed using canonical genes *Zbtb46* and *Flt3*, whereas monocytes and T cell zone macrophages (TZ macrophages), which are unable to prime $CD4^+$ T_{conv} (Baratin et al., 2017), both occupied cluster 5, localizing to opposite sides of the cluster (Figure S1C).

We performed differential expression (DE) analysis for each myeloid cluster versus all other clusters and generated heatmaps for the top 10 most differentially expressed genes (Figure 1C; Table S2). In addition to highlighting key genes contributing to unbiased population segregation, several markers validated previous reports of specialized cellular functions e.g., production of *Il12b* in $mCD103^+$ cDC1(Miller et al., 2012) or *Ccl17* in cDC2 and mLC (Alferink et al., 2003). Moreover, there was a pattern of shared transcriptional identity within resident and migratory populations, which was further defined by DE analysis of migratory (clusters 0, 1, 2, 4, and 6) compared to resident (clusters 3 and 7) DC populations (Figure S1D; Table S3). Expression was largely uniform within migratory and resident DC, with enrichment of genes previously associated with migratory populations such as *Socs2* or *Fscn1* (Miller et al., 2012).

Populations identified through unbiased clustering largely mirrored those identified using gene signatures; however, in contrast to $mCD103^+$ cDC1, the signature for migratory cDC2 applied to multiple clusters indicating substantial heterogeneity. DE analysis between migratory cDC2 clusters 0 and 4 identified specific expression of *Cd9* on cluster 0 (Figure 1D; Table S4). Surface CD9 expression parsed the two cDC2 populations and correlated with CD301b, a previously identified molecule distinguishing cDC2 subsets (Kumamoto et al., 2013), allowing for identification of $CD9^-CD301b^-$ ($mCD301b^-$) and $CD9^+CD301b^+$ ($mCD301b^+$) populations (Figures 1D and S1E). Due to the existing literature and robust staining, CD301b was subsequently used.

CD301b is often expressed by cells of monocyte and macrophage (Mo/Mac) lineage, so we assessed expression of Mo/Mac-related molecules on $mCD301b^-$ and $mCD301b^+$. $mCD301b^-$ and $mCD301b^+$ cells expressed cDC2 markers FLT3 and SIRPα (Miller et al., 2012) and are cDC based on expression of Zbtb46 (Figure S1H) (Meredith et al., 2012; Satpathy et al., 2012). $mCD301b^+$, however, expressed markers associated with cells of a Mo/Mac lineage (Gautier et al., 2012), including CD14, CD16/32 (FcgRIII/II), CD200R, and CD206 (Figure S1F). Furthermore, $mCD301b^+$ expressed higher levels of inhibitory receptors PD-L2 and LILRB4 (Figure S1G).

From this analysis, we derived a flow cytometry panel encompassing this heterogeneity (Figure 1E) and determined the frequency of each population (Figure S1I). We next sought to identify the exact APC(s) responsible for anti-tumor $CD4^+$ T_{conv} priming by using these markers.

Requisite Migration of tdLN Populations

$CD103^+$ cDC1 migration to the tdLN is critical for antitumor $CD8^+$ T cell priming (Roberts et al., 2016), but less is known about cDC2 migration from the tumor. We sought to identify whether these two cDC2 populations were tumor-originating and bore tumor-antigen. Consistent with our scRNA-seq analysis, migratory populations expressed surface CCR7 within the tdLN (Figure S1J), corresponding to migration from the periphery. We then assessed the levels of tumor antigen within myeloid cells of tdLN from B16-ZsGreen ($B16^{ZsGr}$) tumor-bearing animals (Figure 1F) and found that $mCD103^+$, $mCD301b^-$, and $mCD301b^+$ were the dominant $ZsGreen^+$ migratory populations, while resident populations generally had lower and heterogeneous levels, consistent with previous findings (Roberts et al., 2016). Notably, $CD301b^-$ and $CD301b^+$ cDC2 are also present within the TME with fractions of both populations expressing CCR7 (Figure S1K), indicating their migratory capacity. We then generated B16-mCherry-OVA ($B16^{ChOVA}$) tumor-bearing $Ccr7^{-/-}$ mice, which lacked all migratory DC in the tdLN (Figure S2A); in this context, transferred OT-II almost completely failed to proliferate (Figure S2B) confirming that migratory DC populations were critical.

De Novo Priming of $CD4^+$ T_{conv} by cDC2 in the tdLN

To identify which cell(s) directly present antigen and how they influence $CD4^+$ T_{conv} priming, we sorted tdLN myeloid populations from mice bearing $B16^{ChOVA}$ tumors and co-cultured them *ex vivo* with naive OT-II. This demonstrated that both migratory cDC2 supported OT-II expansion based on cell number (Figure 2A) and frequency of division (Figure 2B). Despite similar antigen loading (Figure 1F), $rCD11b^+$ induced little proliferation of

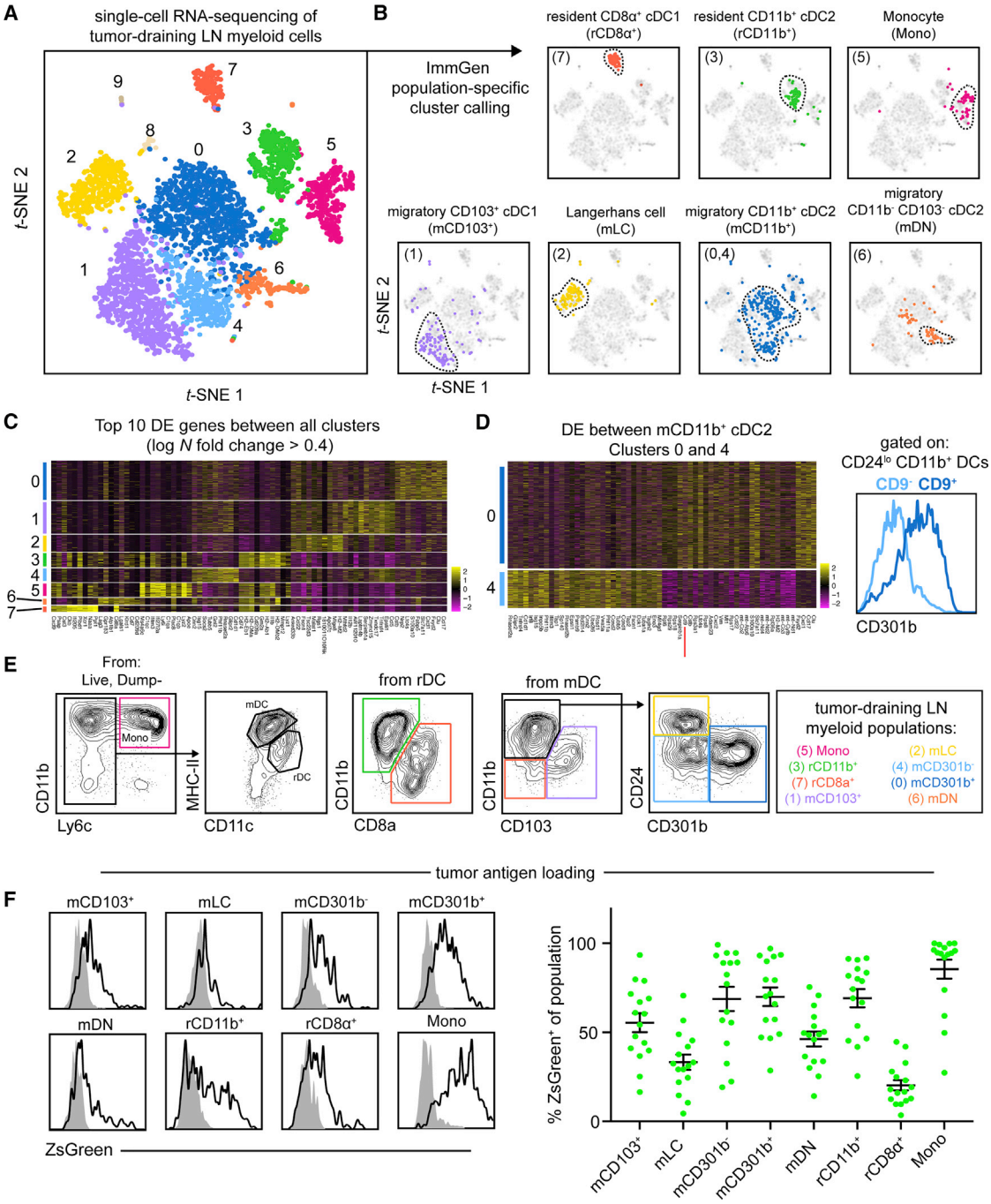

Figure 1. Unbiased scRNA-seq of Myeloid Cells in the tdLN Reveals Extensive Heterogeneity

(A) *t*-SNE display and graph-based clustering of CD90.2$^-$ B220$^-$ NK1.1$^-$ CD11b$^+$ and/or CD11c$^+$ myeloid cells sorted from B16F10 tdLN and processed for scRNA-seq. Each dot represents a single cell.

(B) Expression of ImmGen population-specific gene signatures distributed across *t*-SNE plot of (A).

(C) Heatmap displaying top 10 DE genes for each cluster when comparing clusters 0 through 7 (ranked by fold change).

(D) Left: a heatmap displaying the top 30 DE genes between clusters 0 and 4, with *Cd9* highlighted by a red line. Right: a flow cytometry histogram displaying the differential surface expression of CD301b between CD9$^-$ and CD9$^+$ CD11b$^+$ CD24$^-$ DCs.

(E) Representative gating strategy used to identify myeloid populations in the tdLN.

(F) Representative flow cytometry histograms displaying levels of ZsGreen tumor antigen within myeloid populations in the tdLN (left). Frequency of ZsGreen$^+$ cells within tdLN myeloid populations (right). Data pooled from two independent experiments.

See also Figure S1 and Tables S1, S2, S3, and S4.

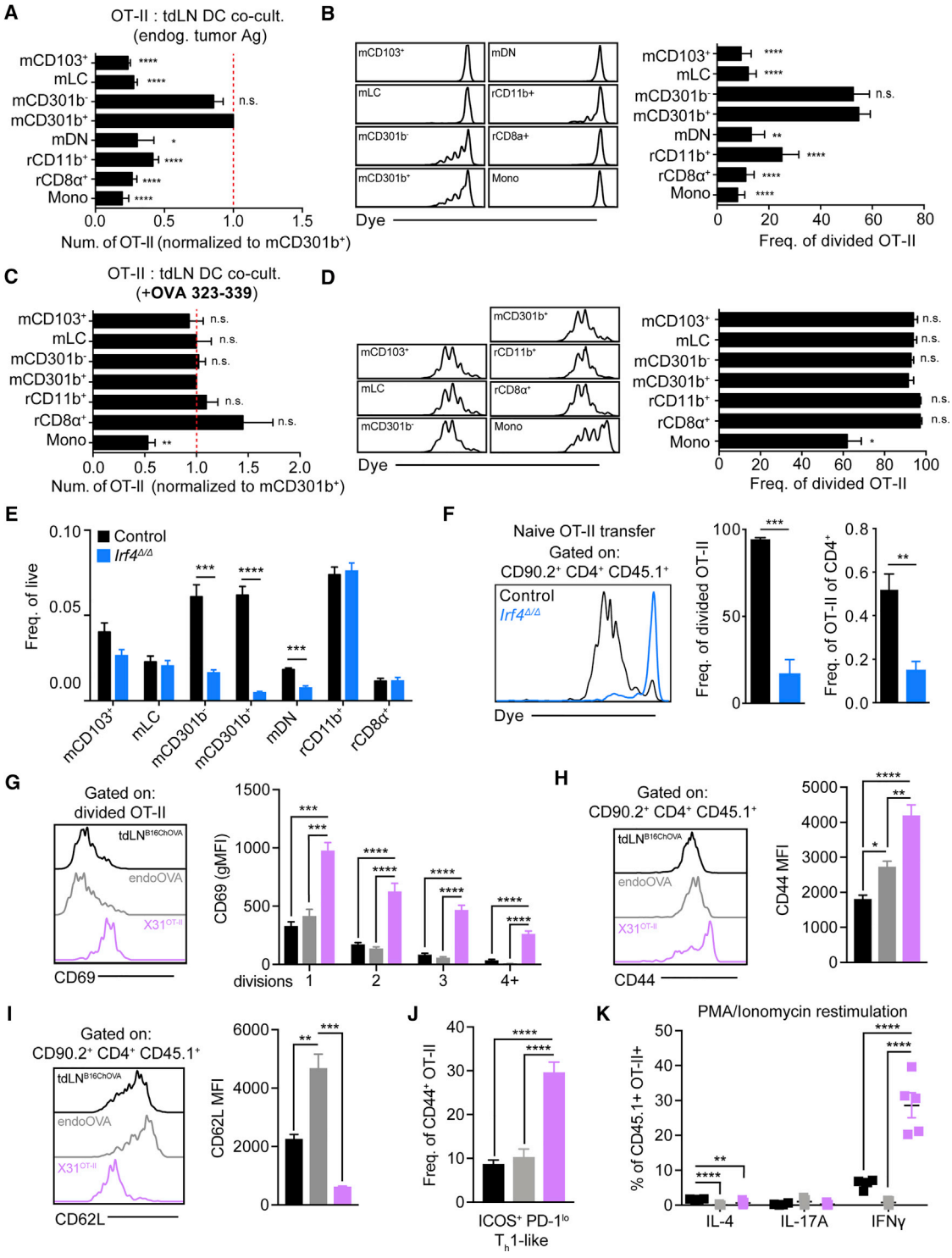

Figure 2. mCD301b$^{-/+}$ cDC2 Are Uniquely Able to Induce Anti-tumor CD4$^+$ T$_{conv}$ Proliferation but Fail to Initiate CD4$^+$ T$_{conv}$ Differentiation

(A–D) OT-II were co-cultured with APC sorted from tdLN of control B78^{ChOVA}-bearing animals and analyzed 3 days after plating.

(A) Absolute number of live OT-II recovered, normalized, and statistically compared to mCD301b$^+$ condition.

(B) Histograms of OT-II dye dilution (left). Frequency of recovered OT-II that had undergone division with statistical comparison to mCD301b$^+$ condition (t test) (right).

(C) Absolute number of live OT-II recovered from co-culture containing exogenous OVA peptide (323–339), normalized and statistically compared to mCD301b$^+$ condition.

(legend continued on next page)

OT-II cells. Addition of exogenous OVA peptide ($OVA_{323–339}$) resulted in comparable proliferation by all populations, confirming their viability and capacity to engage $CD4^+$ T_{conv}; these populations likely do not process and present tumor antigen on MHC-II, restricting their ability to prime $CD4^+$ T_{conv} (Figures 2C and 2D).

To test whether cDC2 were required *in vivo* for initiating $CD4^+$ T_{conv} priming, mice deficient in *Irf4* in DC, which lack LN cDC2 (Krishnaswamy et al., 2017), were used. Use of *Irf4*$^{flox/flox}$*Itgax*^{Cre} resulted in spontaneous germline deficiency (data not shown) preventing us from deleting *Irf4* specifically in myeloid cells. Instead, we used globally deficient *Irf4*$^{\Delta/\Delta}$ (*Irf4*$^{flox/flox}$*ActB*^{Cre}) B16^{ChOVA}-tumor-bearing animals that had reduced numbers of all migratory cDC2 populations in the tdLN (Figure 2E). Transferred CD45.1$^+$ OT-II in *Irf4*$^{\Delta/\Delta}$ mice failed to proliferate and accumulate in the tdLN (Figure 2F) while in *Xcr1*^{DTR} mice, depletion of cDC1 did not impact OT-II proliferation (Figures S2C and S2D). As *Cx3cr1* is differentially expressed by rCD11b$^+$ (Table S2), we generated *Cx3cr1*$^{lsl\text{-}DTR}$*CD11c*^{Cre} animals that allowed specific depletion of rCD11b$^+$ (Figure S2E); depletion of rCD11b$^+$ similarly did not reduce OT-II proliferation (Figure S2F). Both *in vitro* and *in vivo* migratory cDC2 are thus the primary inducers of antitumoral $CD4^+$ T_{conv} priming.

Tolerogenic $CD4^+$ T_{conv} Priming in the tdLN

In tumor-bearing mice, despite evident initiation of $CD4^+$ T_{conv} priming, anti-tumor immunity is ineffective. We thus hypothesized that $CD4^+$ T_{conv} may not be differentiating to effectors and directly compared *in vivo* activation and differentiation of transferred OT-II in the tdLN (tdLN^{B16ChOVA}), in a tolerizing LN via injection of adjuvant-free antigen (endoOVA) and with inflammation-inducing influenza virus (X31^{pOVA}). CD69 expression on OT-II at day 3, indicating strength of T cell activation (Allison et al., 2016) and/or exposure to inflammatory cytokines (Shiow et al., 2006), was similar in tdLN^{B16ChOVA} and tolerizing endoOVA and much lower as compared to X31^{pOVA} (Figure 2G). X31^{pOVA} infection induced potent activation markers on OT-II, namely CD44 upregulation and CD62L downregulation, which was not observed to the same extent on tdLN^{B16ChOVA} OT-II nor endo^{OVA} OT-II (Figures 2H and 2I).

Finally, we found minimal ICOS$^+$PD-1^{lo} T_h1 differentiation in both tdLN^{B16ChOVA} and endo^{OVA} conditions at day 7, compared to X31^{pOVA} (Figure 2J) coinciding with minimal cytokine production following restimulation (Figure 2K). While cDC2 initiate $CD4^+$ T_{conv} priming in the tdLN, defective effector T_{conv} differentiation predicts that therapeutic improvement of $CD4^+$ T_{conv} priming may be possible through alterations in cDC2 phenotype.

Concomitant Expansion of T_{reg} and cDC2 in the TME

While tumor expression of GM-CSF (B16$^{Gm\text{-}csf}$) alters the proportion of cDC2 in the TME (Broz et al., 2014), $CD4^+$ T_{conv} numbers do not rise appreciably with increases in cDC2 (both CD301b$^-$ and CD301b$^+$ subsets) (Figures 3A and S3A). As these cDC2 present antigen to $CD4^+$ T cells (Figure 2), we hypothesized that T_{reg} prefentially expand and act as a feedback mechanism suppressing cDC2 function and antitumor $CD4^+$ T_{conv} priming. We found a positive correlation between T_{reg} and cDC2 frequencies in the TME, and as DC may be inhibited by T_{reg} (Bauer et al., 2014), we tested whether T_{reg} may negatively regulate cDC2 impact on $CD4^+$ T_{conv} differentiation.

Therapeutic Benefits of T_{reg} Depletion Rely on *De Novo* $CD4^+$ T_{conv} Priming

Diphtheria toxin (DT) treatment of *Foxp3*^{DTR} mice (Kim et al., 2007) led to robust T_{reg} depletion and tumor rejection (Figures 3B, S3B, and S3C) that required $CD4^+$ T_{conv} as previously shown (Bos et al., 2013) (Figure 3C). We next tested whether rejection depended on reactivation of $CD4^+$ T_{conv} in the TME or infiltration of new $CD4^+$ T_{conv} from the tdLN. Treatment with the S1PR antagonist FTY720 blocks T cell egress from the tdLN (Chiba et al., 1998) but had little effect on tumor growth. FTY720/DT-treated *Foxp3*^{DTR} mice, however, were unable to reject tumors in contrast to their DT-treated *Foxp3*^{DTR} controls (Figure 3D). Thus, $CD4^+$ T_{conv} tdLN priming and egress is required for tumor rejection following T_{reg} depletion.

T_{reg} Depletion Induces Enhancement of Both cDC2 and $CD4^+$ T_{conv}

Transferred OT-II in B16^{ChOVA} tumor-bearing T_{reg}-deplete animals showed enhanced expansion in the tdLN at day 3 (Figure 3E), and we hypothesized that T_{reg} depletion relieved suppression of the cDC2/$CD4^+$ T_{conv} axis. Thus, we examined DC antigen trafficking to the tdLN following T_{reg} depletion in B16^{ZsGr} tumor-bearing mice. Following T_{reg} depletion, ZsGreen$^+$ mCD301b$^-$ and mCD301b$^+$ in the tdLN were greatly increased in number while other migratory populations were only weakly increased or unchanged (Figure 3F). Mice deficient in *Il-10*, *Itgb8* (transforming growth factor β1 [TGF-β1]-related), or *Areg* had no change in the number of ZsGreen$^+$ cDC2 in the tdLN

(D) Histograms of OT-II dye dilution (left). Frequency of recovered OT-II that had undergone division with statistical comparison to mCD301b$^+$ condition (t test) (right).

(E) Frequency of tdLN DC populations in control or *Irf4*$^{-/-}$ tumor-bearing mice.

(F) Purified CD45.1$^+$ OT-II were adoptively transferred to control or *Irf4*$^{-/-}$ B16^{ChOVA} tumor-bearing mice with tdLN harvested 3 days later to assess OT-II dye dilution (left) and quantify the OT-II that divided (middle) and their frequency (right).

(G–K) CD45.1$^+$ OT-II were transferred to wild-type mice that were inoculated with B16^{chOVA} (tdLN^{B16ChOVA}), endoOVA, or X31^{pOVA} and draining LNs were harvested for analysis.

(G) Histogram of CD69 on divided CD45.1$^+$ OT-II (left) and quantification of MFI with each cell division as determined by dye dilution (right) 3 days following transfer.

(H and I) Surface CD44 (H) and CD62L (I) levels on transferred CD45.1$^+$ OT-II (left) and quantification of MFI (right) 3 days following transfer.

(J) Frequency of transferred CD45.1$^+$ CD44$^+$ OT-II that are ICOS$^+$PD-1^{lo} T_h1-like.

(K) Frequency of transferred CD45.1$^+$ CD44$^+$ OT-II that produce interleukin (IL)-4, IL-17A, and IFNγ following *ex vivo* restimulation 7 days after transfer. Data are represented as average ± SEM unless explicitly specified. *p < 0.05, **p < 0.01, ***p < 0.001, ****p < 0.0001.

See also Figure S2.

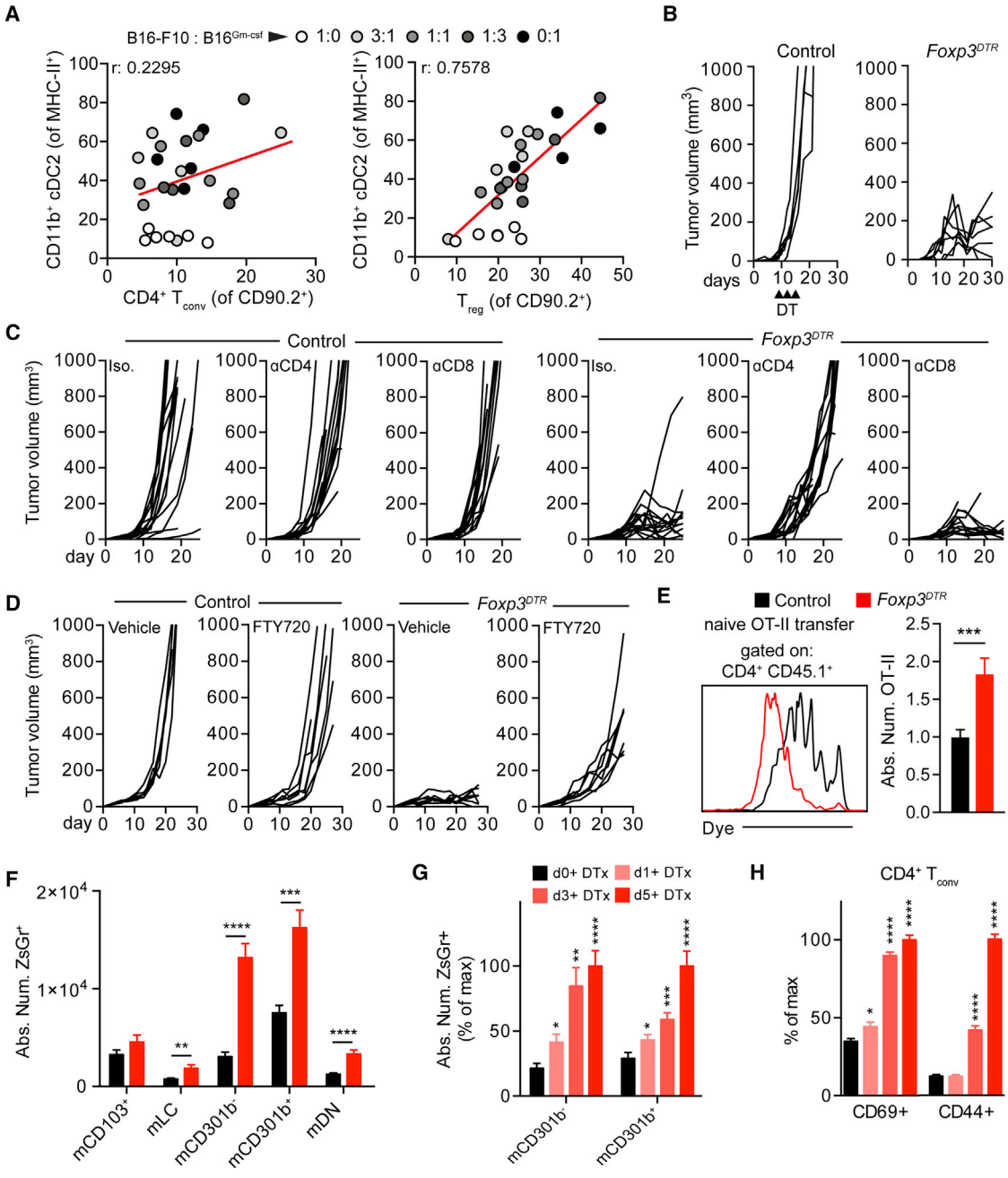

Figure 3. T_{reg} Depletion Enhances cDC2 Migration to the tdLN and Unleashes an Anti-tumor $CD4^+$ T_{conv} Response

(A) Correlation of intratumoral $CD11b^+$ $CD301b^{-/+}$ cDC2 frequency compared to $CD4^+$ T_{conv} (left) or T_{reg} (right). Dots colored according to ratio of B16-F10:$B16^{Gmcsf}$ cells in the tumor. Two pooled experiments displayed.

(B) Tumor growth from control and *Foxp3*^{DTR} mice. Black arrowheads indicate DT treatment. Results depict tumor growth curves of individual mice.

(C) Tumor growth from control or *Foxp3*^{DTR} mice injected with depleting antibodies. Results depict tumor growth curves of individual mice. Two pooled experiments displayed.

(D) Tumor growth from control or *Foxp3*^{DTR} mice injected with with vehicle or FTY720. Results depict tumor growth curves of individual mice. Two pooled experiment displayed.

(E) $CD45.1^+$ OT-II T cells were adoptively transferred into DT-treated control or *Foxp3*^{DTR} $B16^{ChOVA}$-tumor-bearing mice and recovered 3 days later for analysis of dye dilution (left) and quantification of absolute number of OT-II present within the tdLN (right). Three pooled experiments displayed with normalization to control.

(F) Absolute number of $ZsGreen^+$ migratory DC in the tdLN of control and *Foxp3*^{DTR} $B16^{ZsGreen}$ tumor-bearing analyzed at day 5 post-DT.

(G) Absolute number of $ZsGreen^+$ migratory DC in the tdLN of control and *Foxp3*^{DTR} $B16^{ZsGreen}$ tumor-bearing analyzed at days 0, 1, 3, and 5 post-DT. Data displayed as percent of maximum absolute number. Samples statistically compared to day 0 DT.

(legend continued on next page)

(Figures S4A–S4C) showing these molecules were not the mechanism of T_{reg} suppression. Trafficking of tumor cDC2, however, depended upon chemokine signaling as pertussis toxin (PTX) blocked the rise in cDC2 in the T_{reg} deplete condition (Figure S3D). Neither proliferation of cDC2 in the tdLN (Figure S3E) nor frequency of DC precursors in the bone marrow of *Foxp3*^{DTR} mice was altered (Figures S3F and S3G), suggesting the expansion of cDC2 was primarily due to enhanced migration. Furthermore, a wave of enhanced cDC2 migration (Figure 3G) coincided with increases in T cell activation markers CD69 and CD44 (Figures 3H and S3H) consistent with newly arriving cDC2 capable of improved T_{conv} priming quality.

To test whether tdLN APC populations in the absence of T_{reg} were capable of priming CD4$^+$ T_{conv}, we co-cultured APC isolated from *Foxp3*^{DTR} tdLN with OT-II *ex vivo* and measured their proliferation. mCD301b$^-$ and mCD301b$^+$ remained the only cells able to support OT-II division and accumulation (Figures 4A and 4B), while other APC still could prime OT-II if provided OVA peptide (Figure S5A). Preliminary results also indicate that in the absence of $T_{reg,}$ cDC2 were critical for inducing enhanced OT-II proliferation *in vivo* (Figures S5B and S5C). By crossing *Xcr1*^{DTR} with *Foxp3*^{DTR}, we further confirmed that cDC1 populations were not required for improved CD4$^+$ T_{conv} priming and tumor rejection following T_{reg} depletion (Figures S5D–S5F). To determine whether cDC2 in the absence of T_{reg} primed more effectively, we measured CD69 expression on divided OT-II co-cultured with cDC2 *in vitro* (Figure 4C) and on divided OT-II transferred *in vivo* (Figure S5G). In both settings, similar to OT-II in X31^{pOVA} (Figure 2), primed OT-II had increased expression of CD69 compared to in control tdLN.

We then performed scRNA-seq of Foxp3^{DTR} tdLN to measure transcriptional changes in cDC2. This confirmed normal representation of myeloid populations within the *Foxp3*^{DTR} tdLN (Figure S5H) and comparable UMI within each cluster (Figure S5I). Comparing gene expression differences between mCD301b$^-$ and mCD301b$^+$ from *Foxp3*^{DTR} tdLN showed that mCD301b$^-$ expressed higher levels of costimulatory molecules in addition to key CD4$^+$ T_{conv} chemoattractant chemokines, while mCD301b$^+$ expressed higher levels of AP-1 family members (Figure S5J; Table S5). We then aggregated scRNA-seq data from tdLN and *Foxp3*^{DTR} tdLN and performed DE analysis on mCD301b$^-$ and mCD301b$^+$ from the two conditions and found pronounced increases in genes involved in costimulation (*Cd80*, *Cd86*), T cell chemoattraction (*Ccl17*, *Ccl22*), and those expressed in response to pro-inflammatory cytokines (*Stat1*, *Stat4*) on cDC2 in *Foxp3*^{DTR} tdLN (Figure 4D; Table S5). The increase in expression of both *Cd80* and *Cd86* was verified by flow cytometry (Figure 4E) and was also increased on other DC populations (Figure S5K).

We next assessed whether this coincided with improved CD4$^+$ T_{conv} cell differentiation *in vivo*. We observed profound increases in CD44$^+$ICOS$^+$PD-1^{lo} T_h1-like cells in the tdLN and tumor following T_{reg} depletion, similar to that seen in X31^{pOVA} (Figures 2, 4F, and 4G), and these cells expressed T-bet (Figure S4L). Loss of expression of *Il-10*, *Itgb8*, or *Areg* had minimal impact on the proportion of ICOS$^+$PD-1^{lo} T_h1-like cells in the tdLN (Figures S4A–S4C), confirming that T_{reg} utilize another mechanism to suppress the cDC2/CD4$^+$ T_{conv} axis.

To confirm T_h1-like cells arise from *de novo* priming and differentiation, we treated control and *Foxp3*^{DTR} mice with DT and FTY720. While FTY720 had minimal impact in control tdLN, treatment of *Foxp3*^{DTR} mice led to increases of T_h1-like cells in tdLN (Figure 4H) and a precipitous drop in the TME (Figure 4I), indicating that the expansion of tumor T_h1-like CD4$^+$ T_{conv} in untreated *Foxp3*^{DTR} mice was due to tdLN priming.

Anti-CTLA-4-Based Therapies Function to Induce Expansion and Functional Enhancement of cDC2

We hypothesized that T_{reg} depletion within the TME specifically was critical for enhanced cDC2 migration and CD4$^+$ T_{conv} differentiation. Thus, we selectively depleted intratumoral T_{reg} (Selby et al., 2013) in B16^{ZsGreen} tumor-bearing animals using a depleting anti-CTLA-4 clone that reduced T_{reg} within the TME but not the tdLN (Figure 5A). This clone, but not a non-depleting anti-CTLA-4 clone (Figures S6A–S6C), led to increased migration of mCD301b$^+$ to the tdLN (Figure 5B) and a significant increase in ICOS$^+$ PD-1^{lo} CD4$^+$ T_{conv} in the tdLN and tumor (Figure 5C). Furthermore, levels of CD80 and CD86 were only increased on cDC2 upon depletion of T_{reg} within the TME (Figures S6D and S6E). These data support T_{reg} depletion in the TME as the primary enhancer of cDC2 migration and function.

As GM-CSF can induce cDC2 expansion, we hypothesized that combination of GVAX (irradiated B16$^{Gm\text{-}csf}$) and anti-CTLA-4 therapy would potentiate CD4$^+$ T_{conv} immunity through expansion of cDC2 and release of their suppression through T_{reg} depletion at the vaccine site. We compared the immune composition of the vaccine site between BVAX (irradiated B16-F10) ± anti-CTLA-4 and GVAX ± anti-CTLA-4. In either GVAX condition, we observed significant increases of both cDC2 subsets (Figure 5D), but anti-CTLA-4 treatment led to a reduction in T_{reg} and expansion of CD4$^+$ $T_{conv.}$ (Figure 5E). GVAX and anti-CTLA-4 functionally enhanced cDC2, increasing both CD80 and CD86 on mCD301b$^-$ within the vaccine-draining LN (vaxLN), whereas mCD301b$^+$ benefitted primarily from GVAX alone (Figure 5F), suggesting that T_{reg} may more specifically suppress CD301b$^-$ cDC2. When we compared tumor growth between BVAX ± anti-CTLA-4 and GVAX ± anti-CTLA-4, we observed that BVAX alone or in combination with anti-CTLA-4 was ineffective at inducing robust antitumor immunity. In contrast, GVAX combined with anti-CTLA-4 lead to a reduction in tumor growth rates (Figure 5G). To assess cDC2 dependency for CD4$^+$ T_{conv} priming in a GVAX setting, we analyzed cDC composition in the vaccine site and vaxLN of control and *Irf4*$^{\Delta/\Delta}$ mice treated

(H) Control and *Foxp3*^{DTR} B16^{ZsGreen} tumor-bearing mice were analyzed for the frequency of CD4$^+$ T_{conv} expressing CD69 and CD44 at days 0, 1, 3, and 5 post-DT. Data displayed as frequency of maximum expression. Samples statistically compared to day 0 DT condition. Data are represented as average ± SEM. *p < 0.05, **p < 0.01, ***p < 0.001, ****p < 0.0001.
See also Figures S3 and S4.

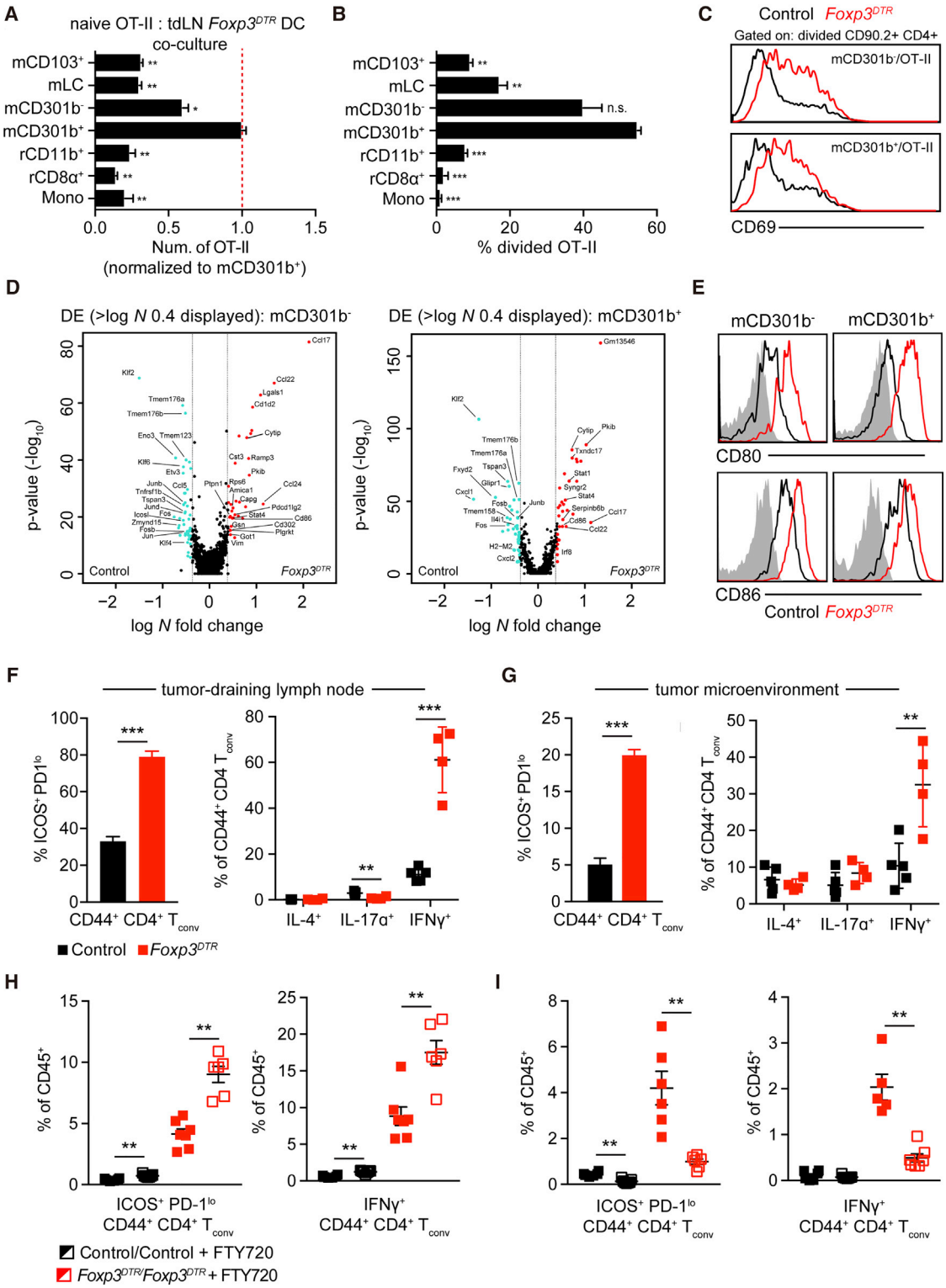

Figure 4. T_{reg} Depletion Enhances cDC2 Function and $CD4^+$ T_{conv} Differentiation

(A–C) OT-II were co-cultured with APC sorted from tdLN of control or *Foxp3*^{DTR} B78^{ChOVA}-bearing animals and analyzed 3 days after plating.

(A) Absolute number of live OT-II T cells recovered, normalized, and statistically compared to mCD301b$^+$ condition.

(B) Frequency of divided OT-II, statistically compared to mCD301b$^+$ condition (t test).

(C) Histogram of CD69 on divided OT-II.

(legend continued on next page)

with anti-CTLA-4 and a combination of GVAX and irradiated B16^{ChOVA}. Loss of *Irf4* greatly reduced the presence of cDC2 (Figure 5H), which corresponded to a near complete loss of OT-II proliferation in the vaxLN (Figure 5I). Taken together, these data along with our prior findings indicate that cDC2 are active targets of T_{reg}-mediated suppression and are central to the initiation of CD4$^+$ T_{conv} antitumor immunity following therapeutic intervention.

scRNA-Seq of the Human tdLN Reveals Similar Heterogeneity within cDC2 Subset between Mouse and Human

scRNA-seq on normal human blood has shown heterogeneity within cDC2 (Villani et al., 2017), although the existence of these populations within the human tdLN has not been assessed. Thus, we performed scRNA-seq on myeloid cells from a human melanoma-draining LN. Following removal of non-APC cellular contaminants, we observed 7 unique clusters from 1,710 input cells (Figure 6A). Using DE and gene overlays, we established cDC1 (hereby referred to as BDCA-3$^+$ cDC1) as cluster 5 and BDCA-1$^+$ cDC2 as cluster 0 (Figures 6B and 6C; Table S6) with both populations expressing genes similar to those identified previously (Villani et al., 2017). To parse additional heterogeneity, we reclustered BDCA-1$^+$ cDC2 and identified 3 populations (Figure 6D) that were transcriptionally distinct based on DE (Figures 6E and 6F; Table S7). Cluster 0.2 expressed CD1E, SLAMF7, and HLA-DQB2, genes that had been identified on a subset of blood cDC2 (Villani et al., 2017). Cluster 0.3, similar to mCD301b$^+$ cDC2 in mouse, expressed genes associated with cells of a monocyte and macrophage lineage, including CD14, VCAN, and S100A8 and like cluster 0.2, resembled a previously identified cDC2 population (Villani et al., 2017). Cluster 0.1 was enriched for genes associated with cell motility (CORO1A, CRIP1, SEPT6, ANXA6) and may represent cellular status instead of a distinct cellular population. We found that CD14$^-$ BDCA-1$^+$ cDC2 and CD14$^+$ BDCA-1$^+$ cDC2 were also present within the TME of a human head and neck squamous cell carcinoma (HNSC) tumor and both expressed CCR7, indicating their migratory potential (Figure 6G). Our data suggest that cDC2 subsets in human tdLN or TME have similar characteristics to mouse cDC2 subsets.

Parsing the Predictive Nature of BDCA-1$^+$ cDC2 in the Human TME

Our data in mice predict that CD4$^+$ T_{conv} quantity and quality will vary with intratumoral cDC2 and T_{reg} density. To assess this in patients, we analyzed the immune composition of 32 primary tumors from the head and neck region, a tumor type rich in T_{reg} (Mandal et al., 2016) (Figures 6G and S7A). We found three distinct patient TME groups with varied abundance of BDCA-1$^+$ cDC2 or T_{reg} (Figure 7A). As predicted, patient TME with low BDCA-1$^+$ cDC2 demonstrated the lowest level of CD4$^+$ T_{conv} infiltration (Figure 7B). Consistent with T_{reg} suppressing CD4$^+$ T_{conv} immunity through BDCA-1$^+$ cDC2, BDCA-1$^+$ cDC2^{HIGH}/Treg^{LOW} TME had greater CD4$^+$ T_{conv} infiltration than BDCA-1$^+$ cDC2^{HIGH}/T_{reg} ^{HIGH} TME. To ensure that differences in CD4$^+$ T_{conv} were not merely due to a proportional shift, we analyzed CD8$^+$ T cell frequencies that varied independently of either T_{reg} or CD4$^+$ T_{conv} frequency (Figure S7B).

Patients with BDCA-1$^+$ cDC2^{LOW}/Treg^{LOW} TME had CD4$^+$ ICOS^{lo}PD-1^{hi} T_{conv} while CD4$^+$ T_{conv} from BDCA-1$^+$ cDC2^{HIGH}/Treg^{HIGH} TME were ICOS^{mid}PD-1^{hi}, perhaps reflective of cells previously reported (Zappasodi et al., 2018) (Figure 7C). In contrast, CD4$^+$ T_{conv} from BDCA-1$^+$ cDC2^{HIGH}/Treg^{LOW} TME were ICOS^{hi}PD-1^{lo} (Figures 7C, S7C, and S7D). While cancer staging at the time of analysis was similar (Figure 7D), progression-free survival was significantly better in BDCA-1$^+$ cDC2^{HIGH}/Treg^{LOW} TME patients than either of the other two TME classes (Figure 7E). These data suggest that the content of immune infiltrate informs the quality of an immune response (ICOS^{hi}PD-1^{lo} CD4$^+$ T_{conv}) and downstream antitumor immunity (progression-free survival).

The presence of high BDCA-3$^+$ cDC1 and NK cells within melanoma (SKCM) is a prognostic indicator of anti-PD-1 responsiveness (Barry et al., 2018). However, in that study, patients with higher densities of CD4$^+$ T_{conv} were present among responders without higher densities of cDC1. To assess whether BDCA-1$^+$ cDC2 could also contribute to anti-PD-1 responsiveness, we re-analyzed and plotted frequency of BDCA-3$^+$ cDC1 and BDCA-1$^+$ cDC2 (both CD14$^{-/+}$) of HLA-DR (Figure 7F). While non-responder TME were generally lower for DC of both subtypes (Figure S7E), responder TME were divided based on the abundance of either BDCA-3$^+$ cDC1 or BDCA-1$^+$ cDC2. We found that responders high for BDCA-1$^+$ cDC2, compared to responders high for BDCA-3$^+$ cDC1, had a significantly lower proportion of CD8$^+$ T cells but significantly higher CD4$^+$ T_{conv} within their TME (Figure 7G), promoting the hypothesis that these BDCA-1^{HIGH} patients have improved CD4$^+$ T_{conv} activity. We reasoned that BDCA-1$^+$ cDC2 abundance alone may predict CD4$^+$ T_{conv} abundance in melanoma (SKCM), as proportions of T_{reg} were significantly lower than in HNSC. (Figure 7H). These data suggest that classes of human TME can be divided based on the abundance of BDCA-1$^+$ cDC2 and that this can be an

(D) Volcano plots of DE genes comparing control and *Foxp3*^{DTR} tdLN mCD301b$^-$ (left) and mCD301b$^+$ (right). Log *N* fold cutoff of 0.4 used. Genes of interest labeled.
(E) Histogram of CD80 and CD86 on mCD301b$^-$ and mCD301b$^+$ in control and *Foxp3*^{DTR} tdLN.
(F) Frequency of CD44$^+$ CD4$^+$ T_{conv} that are ICOS$^+$ PD-1^{lo} in control and *Foxp3*^{DTR} tdLN (left). Frequency of tdLN CD44$^+$ CD4$^+$ T_{conv} producing IL-4, IL-17A, or IFNγ from control or *Foxp3*^{DTR} tumor-bearing mice following *ex vivo* restimulation (right).
(G) Frequency of CD44$^+$ CD4$^+$ T_{conv} that are ICOS$^+$ PD-1^{lo} in control and *Foxp3*^{DTR} TME (left). Frequency of CD44$^+$ CD4$^+$ T_{conv} producing IL-4, IL-17A, or IFNγ in control or *Foxp3*^{DTR} TME following *ex vivo* restimulation (right).
(H and I) Control and *Foxp3*^{DTR} tumor-bearing mice were treated with FTY720 or vehicle and tdLN (H) or tumor (I) were harvested to quantify frequency of CD45$^+$ cells that are CD44$^+$ CD4$^+$ ICOS$^+$ PD-1^{lo} T_{conv} (left) and are IFNγ-producing CD44$^+$ CD4$^+$ T_{conv} following *ex vivo* restimulation (right). Representative experiment displayed. Data are represented as average ± SEM. *p < 0.05, **p < 0.01, ***p < 0.001, ****p < 0.0001.
See also Figures S4 and S5 and Table S5.

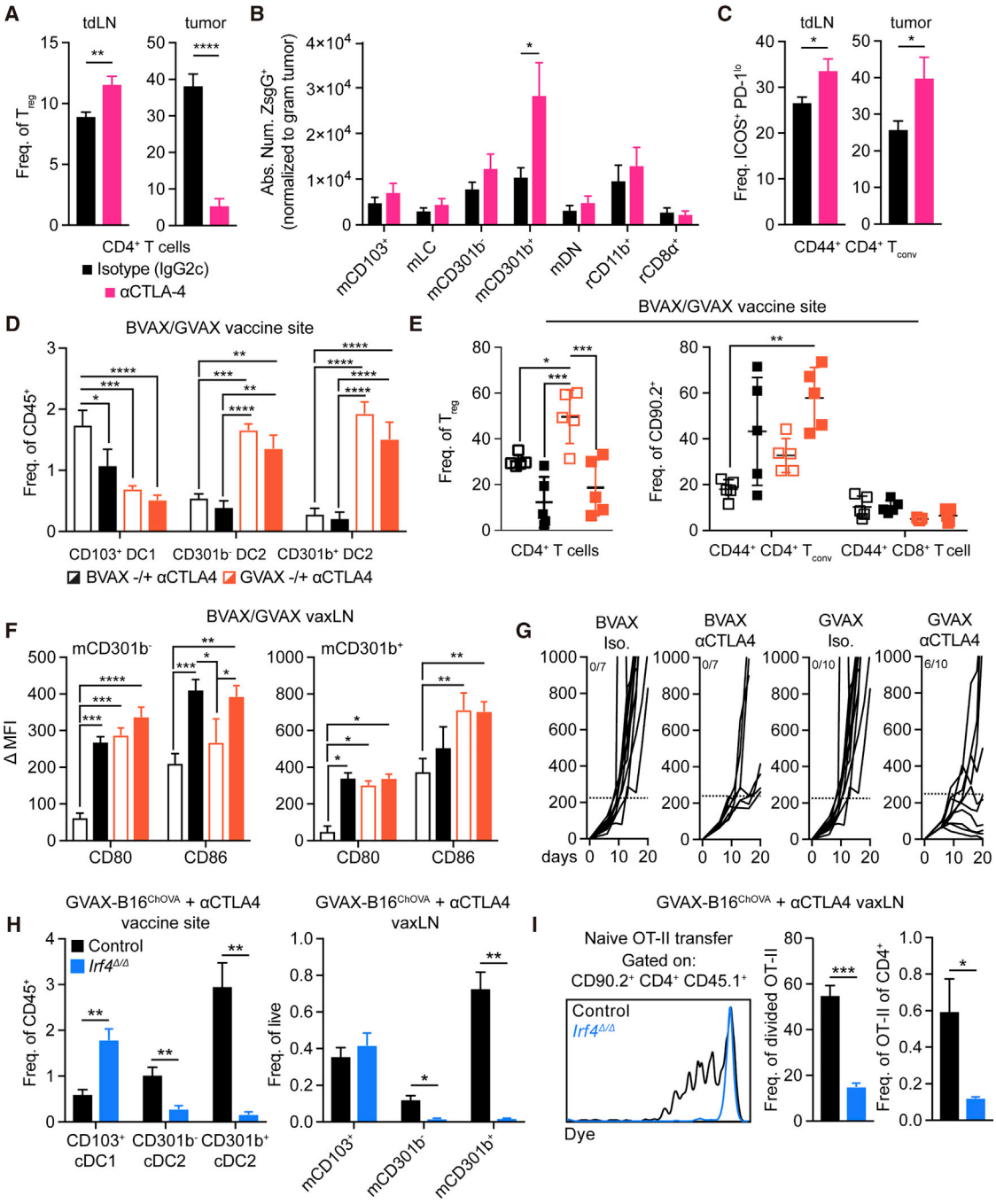

Figure 5. Anti-CTLA-4 Induces Expansion and Functional Enhancement of CD11b$^+$ cDC2

(A) Frequency of T_{reg} within CD4$^+$ T cells in tdLN (left) or tumor (right) from B16^{ZsGreen} tumor-bearing mice treated with mouse isotype or anti-CTLA-4 IgG2c.

(B) Absolute number of ZsGreen$^+$ DC in tdLN (normalized to weight of associated tumor).

(C) Frequency of CD44$^+$ CD4$^+$ T_{conv} with ICOS$^+$ PD-1^{lo} surface phenotype in tdLN (left) or tumor (right).

(D) DC frequency of CD45$^+$ cells within the vaccine site of mice treated with BVAX ± αCTLA-4 or GVAX ± αCTLA-4.

(E) Frequency of T_{reg} among CD4$^+$ T cells (left) and frequency of CD44$^+$ CD4$^+$ T_{conv} or CD44$^+$ CD8$^+$ T cells among CD90.2$^+$ T cells within the vaccine site of mice treated with BVAX ± αCTLA-4 or GVAX ± αCTLA-4 (right).

(F) Quantification of CD80 and CD86 ΔMFI on mCD301b$^-$ (left) or mCD301b$^+$ (right) within the vaxLN of mice treated with BVAX ± αCTLA-4 or GVAX ± αCTLA-4.

(G) Tumor growth from mice treated with BVAX ± αCTLA-4 or GVAX ± αCTLA-4. Ratio represents number of mice with tumors that displayed profound response (<250 mm^3 dotted line). Representative experiment displayed.

(H) DC frequency of either CD45$^+$ or live cells within the vaccine site (left) or vaxLN (right) of control or *Irf4*$^{Δ/Δ}$ mice treated with GVAX-B16^{ChOVA} and anti-CTLA-4.

(legend continued on next page)

indicator for both CD4$^+$ T_{conv} quality and to identify patients who are likely to respond to ICB.

DISCUSSION

Here, we define the cell type(s) necessary for *de novo* priming of new antitumor CD4$^+$ T_{conv}. A fundamental conclusion is that MHC-II presentation of peptides to prime naive CD4$^+$ T_{conv} is heavily biased to cDC2, with the phenotype of these cells distinguishing tumor control versus tumor tolerance. CD4$^+$ T_{conv} priming in tdLN most resembles that of non-inflamed lymph nodes, where CD4$^+$ T_{conv} are generated with a depressed activation state, with little or no evidence of the Th1-like ICOS$^+$ PD-1^{lo} phenotype (Figure 2). While the TME may further drive exhaustion, this conclusion suggests that efficacy of immunotherapies for CD4$^+$ T_{conv} will rely on modulation of this defective step of priming. Indeed, given the apparent irreversibility of certain forms of exhaustion (Philip et al., 2017), it is possible that the efficacy of ICB is linked to ongoing *de novo* lymph node priming rather than only blockade of checkpoint ligands in the tumor.

Our scRNA-seq and functional data demonstrate that two distinct populations of IRF4-dependent cDC2—for which we found homologs in human tdLN and TME—are required *in vivo* for initiating activation of antitumor CD4$^+$ T_{conv}. The complement of myeloid cells identified in mouse tdLN are consistent with previous reports (Salmon et al., 2016) with our approach assaying all populations in parallel to unambiguously confirm of CD4$^+$ T_{conv} stimulatory function. Our data suggest mCD301b$^-$ and mCD301b$^+$ play largely redundant roles in antitumor immunity as each population was capable of supporting comparable OT-II proliferation *ex vivo* and collectively *in vivo* (Figure 2), although we cannot exclude the possibility that these cell populations have disparate functions in other tumor models or following different treatments. cDC2 have been previously associated with CD4$^+$ T_{conv} priming. CD301b$^+$ cDC2 specifically induce T_h2 response to adjuvant (Kumamoto et al., 2013) and a second study demonstrated that pan-cDC2 population in tumor could induce T_h17 differentiation, though we do not observe notable T_h17 skewing in our study (Laoui et al., 2016). Our findings specifically document suboptimal triggering of early T cell activation (e.g., CD69, CD44 levels) as well as poor induction of OT-II effector differentiation in tdLN and non-inflamed LN compared to inflammatory conditions such as influenza or Treg-depletion (Figure 2). Previous work has identified an interferon (IFN)γ-dependent homeostatic 200 gene program associated with poor DC:T cell priming, some of which is co-opted in tumors (Nirschl et al., 2017). We also found expression of some of these genes in tdLN mDC (e.g., *Socs2*, *Fscn1*) (Figure 1) and were able to further define a functional readout for phenotypic defects in cDC2. Whether these genes underlie T_{reg}-mediated suppression or defects in CD4$^+$ T_{conv} differentiation is unclear, although these data support a homeostatic phenotypic dampening of cDC function, particularly in cDC2, that can be reverted during specific inflammatory settings.

Both systemic and tumor-specific therapeutic depletion of T_{reg} enhanced cDC2 migration and reverted phenotypic dysfunction, which in turn allowed productive antitumor CD4$^+$ T_{conv} priming in the tdLN. Previous studies have demonstrated reactivated CD4$^+$ T_{conv} immunity following T_{reg}-depletion (Bos et al., 2013), although the mechanism through which reactivation occurred was unknown. While we cannot preclude the possibility that T_{reg} suppress CD4$^+$ T_{conv} directly (Pandiyan et al., 2007) or impact DC more generally (Bauer et al., 2014), our data demonstrate a potently immunosuppressive relationship between T_{reg} and cDC2. Expansion of cDC2, in either the TME (Figure 3) or GVAX site (Figure 5), induces concurrent increases in T_{reg} that likely promote continued cDC2 suppression, opposing their ability to drive productive priming of effector CD4$^+$ T_{conv}. Enhanced cDC2 migration to the tdLN was observed following Treg depletion induced by either genetic or therapeutic means (Figures 3 and 4). While DC upregulate CCR7 in response to inflammatory cues, DC can also migrate continuously under homeostatic conditions (Baratin et al., 2015). Given the rapid migration of cDC2 from tumor to tdLN following T_{reg}-depletion, we suspect that T_{reg} may regulate homeostatic cDC2 trafficking to the tdLN.

Enhanced cDC2 supported better CD4$^+$ T_{conv} priming and improved differentiation to a ICOS$^+$ PD-1^{lo} T_h1-like phenotype (Figures 3 and 4). Although CD103$^+$ cDC1 can induce T_h1 immunity in specific inflammatory settings (Liang et al., 2016), they were dispensable for tumor rejection following T_{reg} depletion, supporting our data demonstrating that cDC2 are uniquely able to initiate productive antitumor CD4$^+$ T_{conv} priming in the absence of T_{reg} (Figure 4). Efficacious anti-CTLA-4 treatment in both mouse and human is associated with the generation of ICOS$^+$ PD-1^{lo} T_h1-like systemically (Fan et al., 2014; Wei et al., 2017), although the site of this population's initial emergence was previously undefined. We found that antitumor ICOS$^+$ PD-1^{lo} CD4$^+$ T_{conv} arise in tdLN during *de novo* priming, and infiltration of these tdLN-derived antitumor CD4$^+$ T_{conv}, as opposed to via local reactivation in the TME, was the dominant mechanism through which tumor rejection occurred (Figures 3 and 4). Together, this highlights the importance of activating cDC2 to improve distal priming for more effective immunotherapy in patients.

In human HNSC TME, we found a remarkable concordance with our murine data whereby heterogeneity in T_{reg} and cDC2 abundance parsed subsets of patients with distinct phenotypes, and the relationship between BDCA-1$^+$ cDC2 and T_{reg} informed both the quantity and character of CD4$^+$ T_{conv}. This parallel strongly suggests that a similar mechanism of T_{reg}-mediated suppression exists in human. The use of T_{reg} alone as a prognostic indicator has varying levels of predictive power (Shang et al., 2015), which may in part be that low T_{reg} abundance fails to differentiate cohorts that have or lack requisite cDC2

(I) Purified CD45.1$^+$ OT-II were adoptively transferred to control or *Irf4*$^{\Delta/\Delta}$ mice treated with GVAX-B16^{ChOVA} and anti-CTLA-4 and vaxLN were harvested 3 days later to assess OT-II dye dilution (left) and quantify the frequency of cells that had divided (middle) and their frequency of endogenous CD4$^+$ T cells (right). Data are represented as ± average SEM. *p < 0.05, **p < 0.01, ***p < 0.001, ****p < 0.0001.
See also Figure S6.

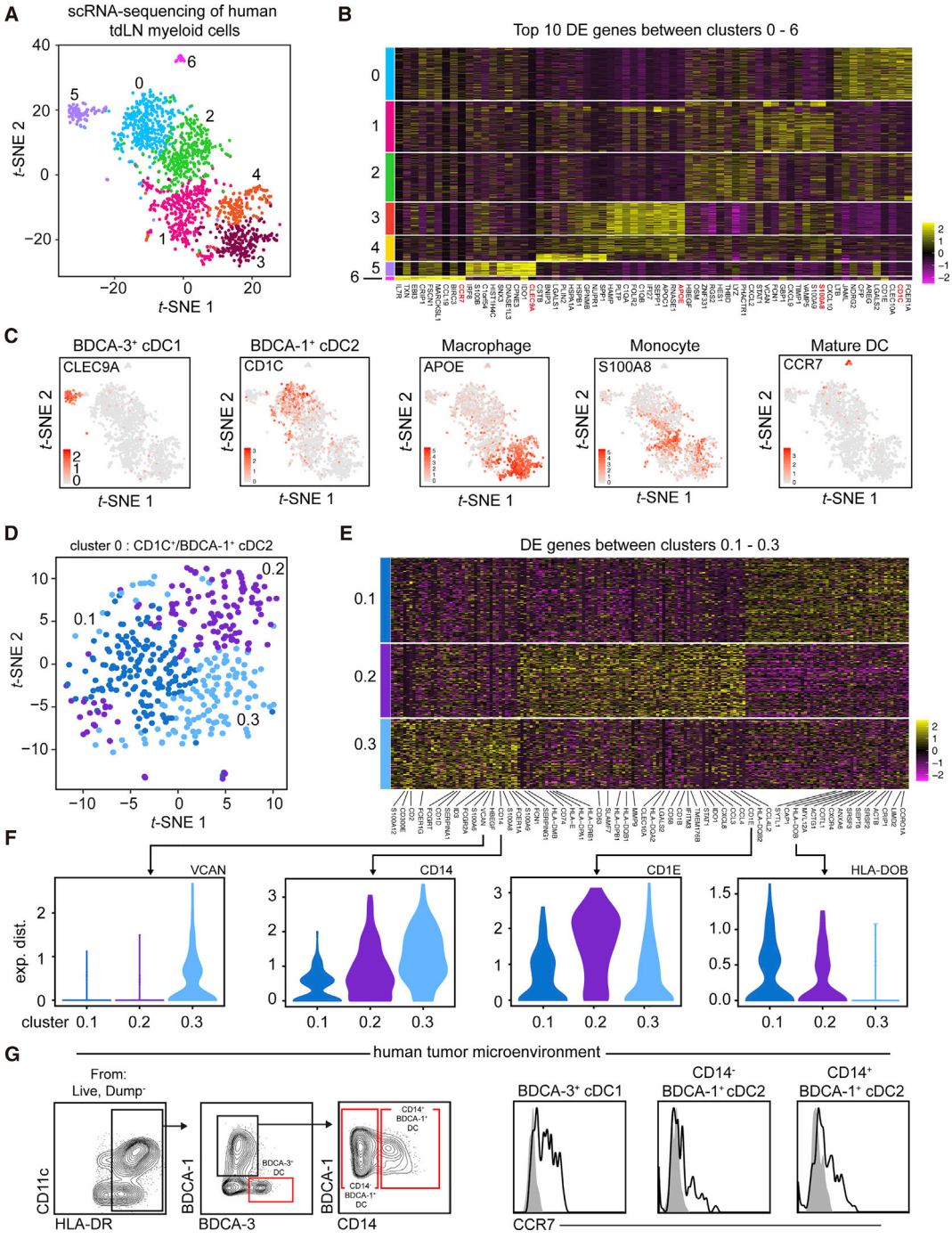

Figure 6. scRNA-Seq of Human Melanoma tdLN Reveals Heterogeneity within BDCA-1⁺ cDC2

(A) *t*-SNE display of CD45⁺ CD3⁻ CD19/20⁻ CD56⁻ myeloid cells sorted from a human melanoma tdLN and processed for scRNA-seq with pDC, neutrophil, NK cell, T cell, and B cell contaminants removed from graph-based clustering analysis.

(B) Heatmap displaying top 10 DE genes for each cluster when comparing clusters 0 through 6 (ranked by fold change).

(C) Gene overlays of markers associated with various myeloid cell types on human tdLN *t*-SNE.

(D) *t*-SNE display and graph-based clustering of BDCA-1⁺ cDC2 (cluster 0) from (A).

(E) Heatmap displaying DE genes between clusters 0.1–0.3 with genes of interested labeled.

(F) Violin plots displaying expression probability differences for denoted genes within clusters 0.1–0.3.

(G) Gating strategy (left) in human TME to identify BDCA-3⁺ cDC1, CD14⁻ BDCA-1⁺ cDC2, and CD14⁺ BDCA-1⁺ cDC2. Cell surface expression of CCR7 on BDCA-3⁺ cDC1, CD14⁻ BDCA-1⁺ cDC2, and CD14⁺ BDCA-1⁺ cDC2 (right).

See also Tables S6 and S7.

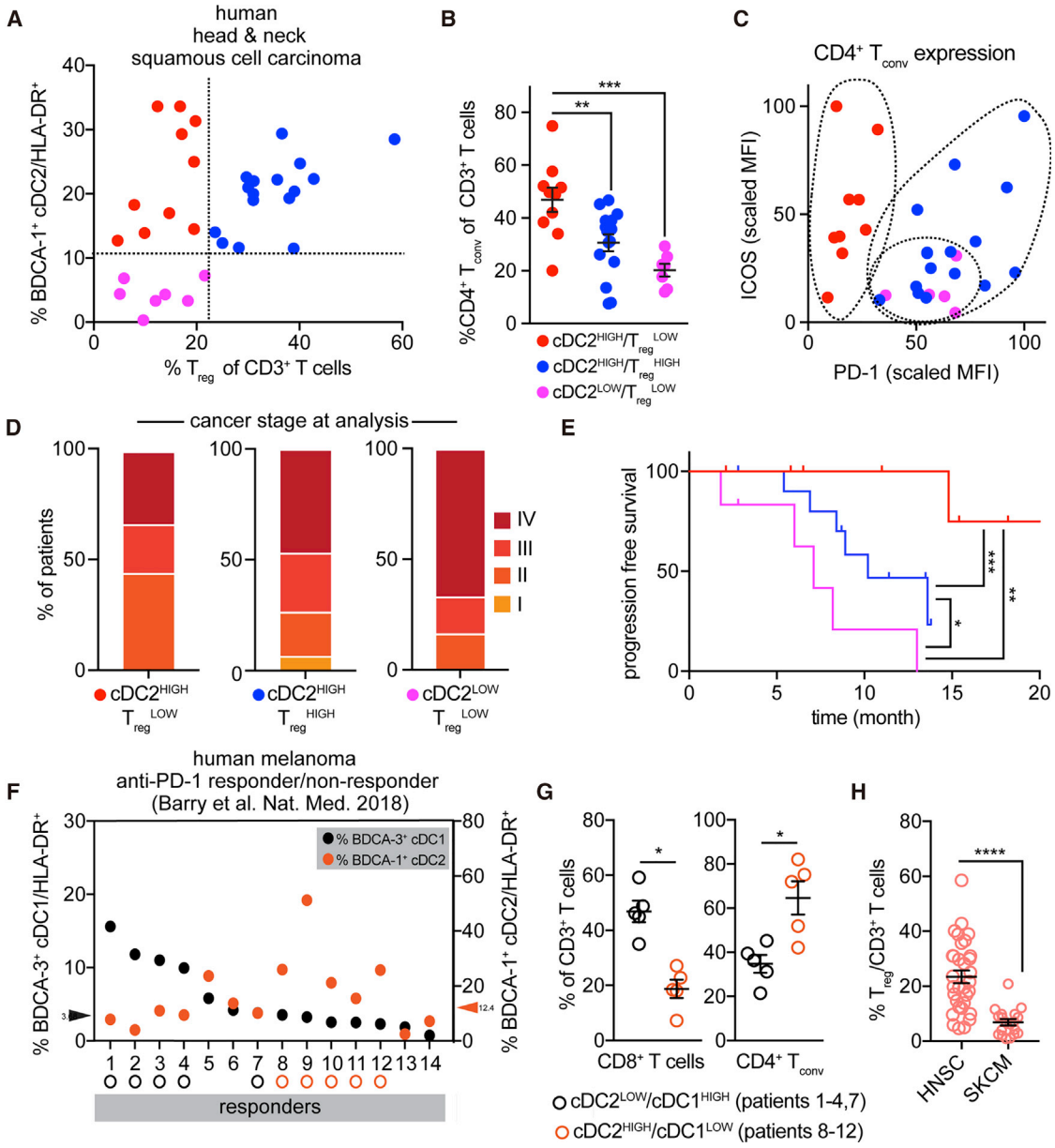

Figure 7. BDCA-1$^+$ cDC2 Proportion in Human TME Impacts CD4$^+$ T_{conv} Proportion and Quality

(A) Dot plot of BDCA-1$^+$ cDC2 frequency of HLA-DR$^+$ cells and T_{reg} frequency of CD3$^+$ T cells as quantified by flow cytometry in 32 human HNSC tumor samples. Dotted lines demarcate samples based on proportion of BDCA-1$^+$ cDC2 (CD14$^{-/+}$) and T_{reg}.

(B) Frequency of CD4$^+$ T cells within each type of TME identified in (A).

(C) Surface expression of ICOS and PD-1 on CD4$^+$ T_{conv}, as a normalized geometric MFI, within each type of human TME identified in (A).

(D) Percent of patients with a given stage of cancer at the time of flow cytometric analysis.

(E) Progression-free survival since disease diagnosis. Mantel-Cox test performed between groups.

(F) 19 human melanoma tumor samples (14 anti-PD-1 responder, 5 anti-PD-1 non-responders; see Figure S6E) were ordered based on abundance of BDCA-3$^+$ cDC1 and plotted for proportions of both BDCA-3$^+$ cDC1 (black) and BDCA-1$^+$ cDC2 (orange). Responders were parsed based on those high for either BDCA-3$^+$ cDC1 (above median split of 3.63) or BDCA-1$^+$ cDC2 (above median split of 12.4).

(G) Frequency of CD3$^+$ T cells that are CD8$^+$ T cells (left) and CD4$^+$ T_{conv} (right) from the two groups identified in (F).

(H) Proportions of T_{reg} among CD3$^+$ T cells in samples from HNSC (A–E) and skin cutaneous melanoma (SKCM) (includes anti-PD-1 responders and non-responders) (F and G). Data are represented as ± average SEM. *p < 0.05, **p < 0.01, ***p < 0.001, ****p < 0.0001.

See also Figure S7.

populations for CD4$^+$ T_{conv} priming. Our pairing of T_{reg} abundance with BDCA-1$^+$ cDC2 unmasks heterogeneity of the TME, allowing for significant predictions of immune response quality and disease-free survival (Figure 7). Looking forward, this suggests that BDCA-1$^+$ DC abundance is a biomarker for a primed TME that can respond to ICB or to novel therapies targeting T_{reg} suppression of cDC2. Indeed, a human TME dataset of anti-PD-1 responder and non-responders demonstrated that while BDCA-3$^+$ cDC1 cellularity is largely associated with anti-PD-1 responsiveness (Barry et al., 2018), some patients were surprisingly BDCA-3$^+$ cDC1^{LOW}, but contained higher proportions of BDCA-1$^+$ cDC2 and CD4$^+$ T_{conv}. This patient group suggests that at least in some TME, such as those with tumor cells that express MHC-II (Johnson et al., 2016), CD4$^+$ T_{conv} may be capable of playing a preeminent role in successful antitumor responses.

Taken together, our work highlights cDC2/BDCA-1$^+$ cDC2 as a target of T_{reg} suppression and as a necessary population for directing antitumor CD4$^+$ T_{conv} immunity. Furthermore, cDC2 abundance in the human TME may act as a biomarker for not only CD4$^+$ T_{conv} quality but also as a contributing indicator for ICB responsiveness. Classifying TME based on immune infiltrate has predictive power (Binnewies et al., 2018), and thus recent (Lavin et al., 2017) and future efforts to characterize disparate TME with unbiased high-dimensional techniques will undoubtable prove invaluable for identifying unique classes of patient TME that are profoundly immunosuppressed or poised for therapeutic response.

STAR★METHODS

Detailed methods are provided in the online version of this paper and include the following:

- KEY RESOURCE TABLE
- CONTACT FOR REAGENT AND RESOURCE SHARING
- EXPERIMENTAL MODEL AND SUBJECT DETAILS
  - Human Tumor Samples
  - Mice
  - Tumor cell lines
- METHOD DETAILS
  - Tumor cell injections and tumor growth experiments
  - Single Cell RNA Sequencing (scRNA-Seq)
  - Single Cell Data Processing
  - Cellular Identification and Clustering
  - ImmGen Signature Generation
  - Sequencing Sample Aggregation
  - Mouse Tissue Digestion and Flow Staining
  - Human Tissue Digestion and Flow Staining
  - APC-T cell *In Vitro* Co-Culture Assays
  - Mouse T cell Isolation and *In Vivo* Adoptive T Cell Transfer
  - T Cell Cytokine Analysis
  - *In Vivo* Treatments
- QUANTIFICATION AND STATISTICAL ANALYSIS
  - Statistical analysis
- DATA AND SOFTWARE AVAILABILITY
  - Data Resources

SUPPLEMENTAL INFORMATION

Supplemental Information can be found with this article online at https://doi.org/10.1016/j.cell.2019.02.005.

ACKNOWLEDGMENTS

We thank E. Wan in the Institute for Human Genetics at UCSF for helping prepare samples for scRNA-seq. We would also like to thank the UCSF Parnassus Flow Cytometry Core for maintenance of flow cytometers and sorters, J.J. Engelhardt and Bristol-Myers-Squibb for Fc-modified anti-CTLA-4 antibodies, S.M. Kaech, M. Conti, and M.D. Rosenblum for mouse strains, L. Rodda for advice related to scRNA-seq, and A. Boissonnas, M.L. Broz, and M.B. Headley for guidance, advice, and critical reading of the manuscript. Acquisition and analysis of certain human samples described in this study was partially funded by contributions from AbbVie, Amgen, Bristol-Myers Squibb, and Pfizer. This work was supported in part by the NSF Graduate Research Fellowship Program awarded to M.B and NIH (U54 CA163123, R21CA191428, and R01 CA197363).

AUTHOR CONTRIBUTIONS

M.B., A.M.M., and M.F.K. designed experiments. M.B. and A.M.M. performed experiments unless specified. J.L.P. and C.J.Y. participated in the processing and analysis of scRNA-seq. A.C. participated in the design, preparation, and analysis of experiments and acquired and analyzed data related to human samples. E.A.H and J.T. performed tumor growth experiments. K.K., M.K.R., K.C.B., M.A.A., and E.W.R. participated in experimental preparation and analyzing flow cytometry. A.D., M.S., J.P.G., and P.H. facilitated acquisition of human tumor tissue. V.C. managed the acquisition and profiling of human tumors. M.B., A.M.M., and M.F.K. wrote and revised the manuscript. M.B., A.M.M., E.W.R., and M.F.K. edited the manuscript.

DECLARATION OF INTERESTS

M.F.K. is a founder, board member, and shareholder in Pionyr Immunotherapeutics that develops novel immunotherapeutics based on tuning of myeloid cells. M.B., J.L.P., and M.A.A. are shareholders in Pionyr Immunotherapeutics.

Received: August 10, 2018
Revised: December 8, 2018
Accepted: February 6, 2019
Published: April 4, 2019

REFERENCES

Alferink, J., Lieberam, I., Reindl, W., Behrens, A., Weiss, S., Hüser, N., Gerauer, K., Ross, R., Reske-Kunz, A.B., Ahmad-Nejad, P., et al. (2003). Compartmentalized production of CCL17 in vivo: strong inducibility in peripheral dendritic cells contrasts selective absence from the spleen. J. Exp. Med. *197*, 585–599.

Allison, K.A., Sajti, E., Collier, J.G., Gosselin, D., Troutman, T.D., Stone, E.L., Hedrick, S.M., and Glass, C.K. (2016). Affinity and dose of TCR engagement yield proportional enhancer and gene activity in CD4+ T cells. eLife *5*, e10134.

Baratin, M., Foray, C., Demaria, O., Habbeddine, M., Pollet, E., Maurizio, J., Verthuy, C., Davanture, S., Azukizawa, H., Flores-Langarica, A., et al. (2015). Homeostatic NF-κB Signaling in Steady-State Migratory Dendritic Cells Regulates Immune Homeostasis and Tolerance. Immunity *42*, 627–639.

Baratin, M., Simon, L., Jorquera, A., Ghigo, C., Dembele, D., Nowak, J., Gentek, R., Wienert, S., Klauschen, F., Malissen, B., et al. (2017). T Cell Zone Resident Macrophages Silently Dispose of Apoptotic Cells in the Lymph Node. Immunity *47*, 349–362.

Barry, K.C., Hsu, J., Broz, M.L., Cueto, F.J., Binnewies, M., Combes, A.J., Nelson, A.E., Loo, K., Kumar, R., Rosenblum, M.D., et al. (2018). A natural killer-dendritic cell axis defines checkpoint therapy-responsive tumor microenvironments. Nat. Med. *24*, 1178–1191.

Bauer, C.A., Kim, E.Y., Marangoni, F., Carrizosa, E., Claudio, N.M., and Mempel, T.R. (2014). Dynamic Treg interactions with intratumoral APCs promote local CTL dysfunction. J. Clin. Invest. *124*, 2425–2440.

Bedoui, S., Whitney, P.G., Waithman, J., Eidsmo, L., Wakim, L., Caminschi, I., Allan, R.S., Wojtasiak, M., Shortman, K., Carbone, F.R., et al. (2009). Cross-presentation of viral and self antigens by skin-derived CD103+ dendritic cells. Nat. Immunol. *10*, 488–495.

Behrens, G., Li, M., Smith, C.M., Belz, G.T., Mintern, J., Carbone, F.R., and Heath, W.R. (2004). Helper T cells, dendritic cells and CTL Immunity. Immunol. Cell Biol. *82*, 84–90.

Benjamini, Y., and Hochberg, Y. (1995). Controlling the False Discovery Rate: A Practical and Powerful Approach to Multiple Testing. J. R. Stat. Soc. Series B Stat. Methodol. *57*, 289–300.

Binnewies, M., Roberts, E.W., Kersten, K., Chan, V., Fearon, D.F., Merad, M., Coussens, L.M., Gabrilovich, D.I., Ostrand-Rosenberg, S., Hedrick, C.C., et al. (2018). Understanding the tumor immune microenvironment (TIME) for effective therapy. Nat. Med. *24*, 541–550.

Bos, P.D., Plitas, G., Rudra, D., Lee, S.Y., and Rudensky, A.Y. (2013). Transient regulatory T cell ablation deters oncogene-driven breast cancer and enhances radiotherapy. J. Exp. Med. *210*, 2435–2466.

Broz, M.L., Binnewies, M., Boldajipour, B., Nelson, A.E., Pollack, J.L., Erle, D.J., Barczak, A., Rosenblum, M.D., Daud, A., Barber, D.L., et al. (2014). Dissecting the tumor myeloid compartment reveals rare activating antigen-presenting cells critical for T cell immunity. Cancer Cell *26*, 638–652.

Chiba, K., Yanagawa, Y., Masubuchi, Y., Kataoka, H., Kawaguchi, T., Ohtsuki, M., and Hoshino, Y. (1998). FTY720, a novel immunosuppressant, induces sequestration of circulating mature lymphocytes by acceleration of lymphocyte homing in rats. I. FTY720 selectively decreases the number of circulating mature lymphocytes by acceleration of lymphocyte homing. J. Immunol. *160*, 5037–5044.

Corthay, A., Skovseth, D.K., Lundin, K.U., Røsjø, E., Omholt, H., Hofgaard, P.O., Haraldsen, G., and Bogen, B. (2005). Primary antitumor immune response mediated by CD4+ T cells. Immunity *22*, 371–383.

Dobin, A., Davis, C.A., Schlesinger, F., Drenkow, J., Zaleski, C., Jha, S., Batut, P., Chaisson, M., and Gingeras, T.R. (2013). STAR: ultrafast universal RNA-seq aligner. Bioinformatics *29*, 15–21.

Dranoff, G., Jaffee, E., Lazenby, A., Golumbek, P., Levitsky, H., Brose, K., Jackson, V., Hamada, H., Pardoll, D., and Mulligan, R.C. (1993). Vaccination with irradiated tumor cells engineered to secrete murine granulocyte-macrophage colony-stimulating factor stimulates potent, specific, and long-lasting anti-tumor immunity. Proc. Natl. Acad. Sci. USA *90*, 3539–3543.

Fan, X., Quezada, S.A., Sepulveda, M.A., Sharma, P., and Allison, J.P. (2014). Engagement of the ICOS pathway markedly enhances efficacy of CTLA-4 blockade in cancer immunotherapy. J. Exp. Med. *211*, 715–725.

Gao, Y., Nish, S.A., Jiang, R., Hou, L., Licona-Limón, P., Weinstein, J.S., Zhao, H., and Medzhitov, R. (2013). Control of T helper 2 responses by transcription factor IRF4-dependent dendritic cells. Immunity *39*, 722–732.

Gautier, E.L., Shay, T., Miller, J., Greter, M., Jakubzick, C., Ivanov, S., Helft, J., Chow, A., Elpek, K.G., Gordonov, S., et al.; Immunological Genome Consortium (2012). Gene-expression profiles and transcriptional regulatory pathways that underlie the identity and diversity of mouse tissue macrophages. Nat. Immunol. *13*, 1118–1128.

GeurtsvanKessel, C.H., Willart, M.A., van Rijt, L.S., Muskens, F., Kool, M., Baas, C., Thielemans, K., Bennett, C., Clausen, B.E., Hoogsteden, H.C., et al. (2008). Clearance of influenza virus from the lung depends on migratory langerin+CD11b- but not plasmacytoid dendritic cells. J. Exp. Med. *205*, 1621–1634.

Gutiérrez-Martínez, E., Planès, R., Anselmi, G., Reynolds, M., Menezes, S., Adiko, A.C., Saveanu, L., and Guermonprez, P. (2015). Cross-Presentation of Cell-Associated Antigens by MHC Class I in Dendritic Cell Subsets. Front. Immunol. *6*, 363.

Headley, M.B., Bins, A., Nip, A., Roberts, E.W., Looney, M.R., Gerard, A., and Krummel, M.F. (2016). Visualization of immediate immune responses to pioneer metastatic cells in the lung. Nature *531*, 513–517.

Heng, T.S., and Painter, M.W.; Immunological Genome Project Consortium (2008). The Immunological Genome Project: networks of gene expression in immune cells. Nat. Immunol. *9*, 1091–1094.

Hodi, F.S., Butler, M., Oble, D.A., Seiden, M.V., Haluska, F.G., Kruse, A., Macrae, S., Nelson, M., Canning, C., Lowy, I., et al. (2008). Immunologic and clinical effects of antibody blockade of cytotoxic T lymphocyte-associated antigen 4 in previously vaccinated cancer patients. Proc. Natl. Acad. Sci. USA *105*, 3005–3010.

Johnson, D.B., Estrada, M.V., Salgado, R., Sanchez, V., Doxie, D.B., Opalenik, S.R., Vilgelm, A.E., Feld, E., Johnson, A.S., Greenplate, A.R., et al. (2016). Melanoma-specific MHC-II expression represents a tumour-autonomous phenotype and predicts response to anti-PD-1/PD-L1 therapy. Nat. Commun. *7*, 10582.

Kim, J.M., Rasmussen, J.P., and Rudensky, A.Y. (2007). Regulatory T cells prevent catastrophic autoimmunity throughout the lifespan of mice. Nat. Immunol *8*, 191–197.

Kowalczyk, M.S., Tirosh, I., Heckl, D., Rao, T.N., Dixit, A., Haas, B.J., Schneider, R.K., Wagers, A.J., Ebert, B.L., and Regev, A. (2015). Single-cell RNA-seq reveals changes in cell cycle and differentiation programs upon aging of hematopoietic stem cells. Genome Res. *25*, 1860–1872.

Krishnaswamy, J.K., Gowthaman, U., Zhang, B., Mattsson, J., Szeponik, L., Liu, D., Wu, R., White, T., Calabro, S., Xu, L., et al. (2017). Migratory CD11b^{+} conventional dendritic cells induce T follicular helper cell-dependent antibody responses. Sci. Immunol. *2*, eaam9169.

Kumamoto, Y., Linehan, M., Weinstein, J.S., Laidlaw, B.J., Craft, J.E., and Iwasaki, A. (2013). CD301b^{+} dermal dendritic cells drive T helper 2 cell-mediated immunity. Immunity *39*, 733–743.

Laoui, D., Keirsse, J., Morias, Y., Van Overmeire, E., Geeraerts, X., Elkrim, Y., Kiss, M., Bolli, E., Lahmar, Q., Sichien, D., et al. (2016). The tumour microenvironment harbours ontogenically distinct dendritic cell populations with opposing effects on tumour immunity. Nat. Commun. *7*, 13720.

Lavin, Y., Kobayashi, S., Leader, A., Amir, E.D., Elefant, N., Bigenwald, C., Remark, R., Sweeney, R., Becker, C.D., Levine, J.H., et al. (2017). Innate Immune Landscape in Early Lung Adenocarcinoma by Paired Single-Cell Analyses. Cell *169*, 750–765.

Liang, J., Huang, H.I., Benzatti, F.P., Karlsson, A.B., Zhang, J.J., Youssef, N., Ma, A., Hale, L.P., and Hammer, G.E. (2016). Inflammatory Th1 and Th17 in the Intestine Are Each Driven by Functionally Specialized Dendritic Cells with Distinct Requirements for MyD88. Cell Rep. *17*, 1330–1343.

Macosko, E.Z., Basu, A., Satija, R., Nemesh, J., Shekhar, K., Goldman, M., Tirosh, I., Bialas, A.R., Kamitaki, N., Martersteck, E.M., et al. (2015). Highly Parallel Genome-wide Expression Profiling of Individual Cells Using Nanoliter Droplets. Cell *161*, 1202–1214.

Mandal, R., Şenbabaoğlu, Y., Desrichard, A., Havel, J.J., Dalin, M.G., Riaz, N., Lee, K.W., Ganly, I., Hakimi, A.A., Chan, T.A., and Morris, L.G. (2016). The head and neck cancer immune landscape and its immunotherapeutic implications. JCI Insight *1*, e89829.

Merad, M., Sathe, P., Helft, J., Miller, J., and Mortha, A. (2013). The dendritic cell lineage: ontogeny and function of dendritic cells and their subsets in the steady state and the inflamed setting. Annu. Rev. Immunol. *31*, 563–604.

Meredith, M.M., Liu, K., Darrasse-Jeze, G., Kamphorst, A.O., Schreiber, H.A., Guermonprez, P., Idoyaga, J., Cheong, C., Yao, K.H., Niec, R.E., and Nussenzweig, M.C. (2012). Expression of the zinc finger transcription factor zDC (Zbtb46, Btbd4) defines the classical dendritic cell lineage. J. Exp. Med. *209*, 1153–1165.

Miller, J.C., Brown, B.D., Shay, T., Gautier, E.L., Jojic, V., Cohain, A., Pandey, G., Leboeuf, M., Elpek, K.G., Helft, J., et al.; Immunological Genome Consortium (2012). Deciphering the transcriptional network of the dendritic cell lineage. Nat. Immunol. *13*, 888–899.

Nirschl, C.J., Suárez-Fariñas, M., Izar, B., Prakadan, S., Dannenfelser, R., Tirosh, I., Liu, Y., Zhu, Q., Devi, K.S.P., Carroll, S.L., et al. (2017). IFNγ-Dependent Tissue-Immune Homeostasis Is Co-opted in the Tumor Microenvironment. Cell *170*, 127–141.

Pandiyan, P., Zheng, L., Ishihara, S., Reed, J., and Lenardo, M.J. (2007). CD4+CD25+Foxp3+ regulatory T cells induce cytokine deprivation-mediated apoptosis of effector CD4+ T cells. Nat. Immunol. *8*, 1353–1362.

Pauken, K.E., Sammons, M.A., Odorizzi, P.M., Manne, S., Godec, J., Khan, O., Drake, A.M., Chen, Z., Sen, D.R., Kurachi, M., et al. (2016). Epigenetic stability of exhausted T cells limits durability of reinvigoration by PD-1 blockade. Science *354*, 1160–1165.

Philip, M., Fairchild, L., Sun, L., Horste, E.L., Camara, S., Shakiba, M., Scott, A.C., Viale, A., Lauer, P., Merghoub, T., et al. (2017). Chromatin states define tumour-specific T cell dysfunction and reprogramming. Nature *545*, 452–456.

Ritchie, M.E., Phipson, B., Wu, D., Hu, Y., Law, C.W., Shi, W., and Smyth, G.K. (2015). limma powers differential expression analyses for RNA-sequencing and microarray studies. Nucleic Acids Res. *43*, e47.

Roberts, E.W., Broz, M.L., Binnewies, M., Headley, M.B., Nelson, A.E., Wolf, D.M., Kaisho, T., Bogunovic, D., Bhardwaj, N., and Krummel, M.F. (2016). Critical Role for CD103(+)/CD141(+) Dendritic Cells Bearing CCR7 for Tumor Antigen Trafficking and Priming of T Cell Immunity in Melanoma. Cancer Cell *30*, 324–336.

Salmon, H., Idoyaga, J., Rahman, A., Leboeuf, M., Remark, R., Jordan, S., Casanova-Acebes, M., Khudoynazarova, M., Agudo, J., Tung, N., et al. (2016). Expansion and Activation of CD103(+) Dendritic Cell Progenitors at the Tumor Site Enhances Tumor Responses to Therapeutic PD-L1 and BRAF Inhibition. Immunity *44*, 924–938.

Satija, R., Farrell, J.A., Gennert, D., Schier, A.F., and Regev, A. (2015). Spatial reconstruction of single-cell gene expression data. Nat. Biotechnol. *33*, 495–502.

Satpathy, A.T., Kc, W., Albring, J.C., Edelson, B.T., Kretzer, N.M., Bhattacharya, D., Murphy, T.L., and Murphy, K.M. (2012). Zbtb46 expression distinguishes classical dendritic cells and their committed progenitors from other immune lineages. J. Exp. Med. *209*, 1135–1152.

Schietinger, A., Philip, M., Krisnawan, V.E., Chiu, E.Y., Delrow, J.J., Basom, R.S., Lauer, P., Brockstedt, D.G., Knoblaugh, S.E., Hämmerling, G.J., et al. (2016). Tumor-Specific T Cell Dysfunction Is a Dynamic Antigen-Driven Differentiation Program Initiated Early during Tumorigenesis. Immunity *45*, 389–401.

Selby, M.J., Engelhardt, J.J., Quigley, M., Henning, K.A., Chen, T., Srinivasan, M., and Korman, A.J. (2013). Anti-CTLA-4 antibodies of IgG2a isotype enhance antitumor activity through reduction of intratumoral regulatory T cells. Cancer Immunol. Res. *1*, 32–42.

Shang, B., Liu, Y., Jiang, S.J., and Liu, Y. (2015). Prognostic value of tumor-infiltrating FoxP3+ regulatory T cells in cancers: a systematic review and meta-analysis. Sci. Rep. *5*, 15179.

Shiow, L.R., Rosen, D.B., Brdicková, N., Xu, Y., An, J., Lanier, L.L., Cyster, J.G., and Matloubian, M. (2006). CD69 acts downstream of interferon-alpha/beta to inhibit S1P1 and lymphocyte egress from lymphoid organs. Nature *440*, 540–544.

Thomas, P.G., Brown, S.A., Yue, W., So, J., Webby, R.J., and Doherty, P.C. (2006). An unexpected antibody response to an engineered influenza virus modifies CD8+ T cell responses. Proc. Natl. Acad. Sci. USA *103*, 2764–2769.

Topalian, S.L., Sznol, M., McDermott, D.F., Kluger, H.M., Carvajal, R.D., Sharfman, W.H., Brahmer, J.R., Lawrence, D.P., Atkins, M.B., Powderly, J.D., et al. (2014). Survival, durable tumor remission, and long-term safety in patients with advanced melanoma receiving nivolumab. J. Clin. Oncol. *32*, 1020–1030.

Villani, A.C., Satija, R., Reynolds, G., Sarkizova, S., Shekhar, K., Fletcher, J., Griesbeck, M., Butler, A., Zheng, S., Lazo, S., et al. (2017). Single-cell RNA-seq reveals new types of human blood dendritic cells, monocytes, and progenitors. Science *356*, eaah4573.

Wei, S.C., Levine, J.H., Cogdill, A.P., Zhao, Y., Anang, N.A.S., Andrews, M.C., Sharma, P., Wang, J., Wargo, J.A., Pe'er, D., and Allison, J.P. (2017). Distinct Cellular Mechanisms Underlie Anti-CTLA-4 and Anti-PD-1 Checkpoint Blockade. Cell *170*, 1120–1133.

Zappasodi, R., Budhu, S., Hellmann, M.D., Postow, M.A., Senbabaoglu, Y., Manne, S., Gasmi, B., Liu, C., Zhong, H., Li, Y., et al. (2018). Non-conventional Inhibitory $CD4^{+}Foxp3^{-}PD\text{-}1^{hi}$ T Cells as a Biomarker of Immune Checkpoint Blockade Activity. Cancer Cell *33*, 1017–1032.

STAR★METHODS

KEY RESOURCE TABLE

REAGENT or RESOURCE	SOURCE	IDENTIFIER
Antibodies		
anti-mouse CD11c BV650 (clone N418)	Biolegend	Cat # 117339
anti-mouse/human CD11b BV605 (clone M1/70)	Biolegend	Cat # 101257
anti-mouse CD103 BV421 (clone 2E7)	Biolegend	Cat # 121421
anti-mouse Ly-6C BV711 (clone HK1.4)	Biolegend	Cat # 128037
anti-mouse CD90.2 BV785 (clone 30-H12)	Biolegend	Cat # 105331
anti-mouse/human CD45R/B220 BV785 (clone RA3-6B2)	Biolegend	Cat # 103246
anti-mouse Ly-6G BV785 (clone IA8)	Biolegend	Cat # 127645
anti-mouse Siglec F BV786 (clone E50-2440)	BD Biosciences	Cat # 740956
anti-mouse NK1.1 BV785 (clone PK136)	Biolegend	Cat # 108749
anti-mouse CD24 PE/Cy7 (clone M1/69)	Biolegend	Cat # 101822
anti-mouse MHC-II AF700 (clone M5/114.15.2)	Biolegend	Cat # 107622
anti-mouse CD301b PE or APC (clone URA-1)	Biolegend	Cat # 146814, 146803
anti-mouse CD8a PerCP/Cy5.5 or PE/Cy7 (clone 53-6.7)	Biolegend	Cat # 100734, 100722
anti-mouse F4/80 FITC (clone BM8)	Biolegend	Cat # 123107
anti-mouse CD45 PerCP/Cy5.5 (clone A20)	Biolegend	Cat # 110727
anti-mouse CD197/CCR7 PE	Biolegend	Cat # 120105
anti-mouse CD9 AF647 (clone MZ3)	Biolegend	Cat # 124809
anti-mouse CD135/FLT3 PE (clone A2F10)	Biolegend	Cat # 135305
anti-mouse CD172a/SIRPA PE or AF488 (clone P84)	Biolegend	Cat # 144011,144023
anti-mouse CD14 PE (clone Sa14-2)	Biolegend	Cat # 123309
anti-mouse CD16/32 PE (clone 93)	Biolegend	Cat # 101307
anti-mouse CD200R PE (clone OX110)	Biolegend	Cat # 123907
anti-mouse CD206 PE (clone C068C2)	Biolegend	Cat # 141705
anti-mouse B7-H1 PE (PD-L1/CD274) (clone 10F.9G2)	Biolegend	Cat # 124307
anti-mouse B7-H2 PE (ICOS-L/CD275) (clone HK5.3)	Biolegend	Cat # 107405
anti-mouse B7-H3 PE (CD276) (clone RTAA15)	Biolegend	Cat # 123507
anti-mouse B7-DC (PD-L2/CD273) PE (clone TY25)	Biolegend	Cat # 107205
anti-mouse CD85K (LILRB4) PE	Biolegend	Cat # 144903
anti-mouse CD4 BUV395 (clone GK1.5)	BD Biosciences	Cat # 563790
anti-mouse/rat/human CD278/ICOS APC (clone C398.4A)	Biolegend	Cat # 313510
anti-mouse CD279/PD-1 PE (clone RMP1-14)	Biolegend	Cat # 114118
anti-mouse/human CD44 BV711 (clone IM7)	Biolegend	Cat # 103057
anti-mouse CD69 BV650 (clone H1.2F3)	Biolegend	Cat # 104541
anti-mouse Foxp3 eF450 (clone FJK-16 s)	Thermo Fisher	Cat # 48-5773-82
anti-mouse/rat/human Foxp3 AF647 (clone 150D)	Biolegend	Cat # 320014
anti-mouse IL-4 PE (clone 11B11)	Biolegend	Cat # 504104
anti-mouse IL-17a BV421 (clone TC11-18H10.1)	Biolegend	Cat # 506926
anti-mouse IFNg PE/Cy7 (clone XMG1.2)	Biolegend	Cat # 505825
anti-mouse/human T-bet BV605 (clone 4B10)	Biolegend	Cat # 644817
anti-mouse CD117 APC (clone 2B8)	Biolegend	Cat # 105811
anti-mouse CD115 PerCP/Cy5.5 (clone AFS98)	Biolegend	Cat # 135525
anti-mouse Ly6-G (clone IA8)	Biolegend	Cat # 127603
anti-mouse CD3e (clone 145-2C11)	Biolegend	Cat # 100303

(*Continued on next page*)

Continued

REAGENT or RESOURCE	SOURCE	IDENTIFIER
anti-mouse CD127 (clone A7R34)	Biolegend	Cat # 135005
anti-mouse NK1.1 (clone PK136)	Biolegend	Cat # 108703
anti-mouse/human CD45R (RA3-6B2)	Biolegend	Cat # 103203
anti-mouse TER-119 (clone TER-119)	Biolegend	Cat # 116203
anti-mouse TCR γ/δ (clone GL3)	Biolegend	Cat # 118103
Streptavidin BV421	Biolegend	Cat # 405226
anti-human CD45 APC/e780 (clone HI30)	Thermo Fisher	Cat # 47-0459-42
anti-human CD3e PerCP/e710 (clone OKT3)	Thermo Fisher	Cat # 46-0037-42
anti-human HLA-DR BUV395 (clone G46-6)	BD Biosciences	Cat # 564040
anti-human CD56 BUV737 (clone NCAM16.2)	BD Biosciences	Cat # 564448
anti-human CD4 PE/Dazzle 594 (clone S3.5)	Biolegend	Cat # 100455
anti-human CD8a BV605 (clone RPA-T8)	Biolegend	Cat # 301039
anti-human CD127 BV650 (clone HIL-7R-M21)	BD Biosciences	Cat # 563225
anti-human CD38 AF700 (clone HIT2)	Biolegend	Cat # 303523
anti-human CD25 APC (clone 2A3)	BD Biosciences	Cat # 340939
anti-human CD45RO PE (clone UCHL1)	BD Biosciences	Cat # 561889
anti-human PD-1 BV786 (clone EH12)	BD Biosciences	Cat # 563789
anti-human ICOS BV711 (clone DX29)	BD Biosciences	Cat # 563833
anti-human FoxP3 PE/Cy7 (clone 236A/E7)	Thermo Fisher	Cat # 25-4777-41
anti-human CTLA-4 BV421 (clone BNI3)	BD Biosciences	Cat # 565931
anti-human/mouse/rat Ki67 AF488 (clone SolA15)	Thermo Fisher	Cat # 11-5698-82
anti-human CD19 PerCP/e710 (clone H1B19)	Thermo Fisher	Cat # 45-0199-42
anti-human CD20 PerCP/e710 (clone 2H7)	Thermo Fisher	Cat # 45-0209-42
anti-human CD56 PerCP/e710 (clone CMSSB)	Thermo Fisher	Cat # 46-0567-42
anti-human CD64 BUV737 (clone 10.1)	BD Biosciences	Cat # 564425
anti-human CD11c AF700 (clone 3.9)	Thermo Fisher	Cat # 56-0116-42
anti-human CD16 BV605 (clone 3G8)	Biolegend	Cat # 302039
anti-human CD273/PDL2 BV650 (clone MIH18)	BD Biosciences	Cat # 563844
anti-human/mouse TREM2 APC (clone 237920)	R&D Systems	Cat # FAB17291A
anti-human CD304 PE (clone 12C2)	Biolegend	Cat # 354503
anti-human CD1C/BDCA-1 PE/Cy7 (clone L161)	Biolegend	Cat # 331515
anti-human CD197 BV421 (clone G043H7)	Biolegend	Cat # 353207
anti-human BDCA-3 FITC (clone AD5-14H12)	Miltenyi	Cat # 130-098-843
anti-human PDL1 BV786 (clone MIH1)	BD Biosciences	Cat # 563739
anti-human CD14 BV711 (clone M5E2)	Biolegend	Cat # 301837
PE Rat IgG2a, k Isotype Ctrl Antibody (clone RTK2758)	Biolegend	Cat # 400508
PE Rat IgG1, k Isotype Ctrl Antibody (clone RTK2071)	Biolegend	Cat # 400408
APC Armenian Hamster IgG Isotype Ctrl Antibody (clone HTK888)	Biolegend	Cat # 400912
BV605 Mouse IgG1, k Isotype Ctrl Antibody (clone MOPC-21)	Biolegend	Cat # 400162
BV421 Mouse IgG2a, k Isotype Ctrl Antibody (clone MOPC-173)	Biolegend	Cat # 400259
anti-mouse CD4 InVivoMab (clone GK1.5)	BioXCell	Cat # BE0003-1
anti-mouse CD8 InVivoMab (clone 2.43)	BioXCell	Cat # BE0061
anti-mouse CTLA-4 (CD152) InVivoMab (clone 9H10)	BioXCell	Cat # BE0131
Rat IgG2b, k InVivoMab	BioXCell	Cat # BE0090
Polyclonal Syrian hamster IgG InVivoMab	BioXCell	Cat # BE0087
anti-mouse CD16/32 InVivoMab	BioXCell	Cat # BE0307
anti-mouse CTLA-4 mouse IgG2c (modified clone 9D9)	Bristol-Myers-Squibb	N/A
anti-mouse CTLA-4 mouse IgG1 (modified clone 9D9)	Bristol-Myers-Squibb	N/A

(*Continued on next page*)

Continued

REAGENT or RESOURCE	SOURCE	IDENTIFIER
mouse IgG2c isotype	Bristol-Myers-Squibb	N/A
mouse IgG1 isotype	Bristol-Myers-Squibb	N/A
Normal Rat Serum	Thermo Fisher	Cat # 10710C
Armenian Hamster Serum	Innovative Research	Cat # IGHMA-SER
Biological Samples		
Human tumor samples	UC San Francisco	IRB # 13-12246 and 14-15342
Mouse tissue samples (LN, tumor)	UC San Francisco	IACUC: AN170208
Chemicals, Peptides, and Recombinant Proteins		
Matrigel GFR, Phenol-red free	Corning	Cat # 356231
Collagenase, Type I	Worthington Biochemical	Cat # LS004197
Collagenase, Type IV	Worthington Biochemical	Cat # LS004189
DNase I	Roche	Cat # 10104159001
Liberase TL	Roche	Cat # 5401020001
Human TruStain FcX	Biolegend	Cat # 422302
Zombie Aqua Fixable Viability Kit	Biolegend	Cat # 423102
Zombie NIR Fixable Viability Kit	Biolegend	Cat # 423106
Brilliant Stain Buffer Plus	BD Biosciences	Cat # 566385
Brefeldin A (BFA)	Sigma-Aldrich	Cat # B7651
Phorbol 12-myristate 13-acetate (PMA)	Sigma-Aldrich	Cat # P8139
Ionomycin	Invitrogen	Cat # I24222
Monensin Solution (1000X)	Thermo Fisher	Cat # 00-4505-51
Diphtheria Toxin (unnicked)	List Biological Laboratories	Cat # 150
FTY720	Cayman Chemical Company	Cat # 10006292
eBioscience Cell Proliferation Dye eFluor 670		Cat # 65-0840-85
Ovalbumin Endofit	Invivogen	Cat # Vac-pova
OVA peptide (323-339)	Genscript	Cat # RP10610-1
Critical Commercial Assays		
Chromium Single Cell 3′ Library & Gel Bead Kit V2	10X Genomics	Cat # 120237
BD Cytofix	BD Biosciences	Cat # 554655
Foxp3/Transcription factor staining buffer set	Thermo Fisher	Cat # 00-5523-00
EasySep Mouse $CD4^+$ T Cell Isolation kit	STEMCELL Technologies	Cat # 19852
Experimental Models: Cell Lines		
B16-F10	ATCC	Cat # CRL-6475
B16-ChOVA	UC San Francisco	N/A
B78-ChOVA	UC San Francisco	N/A
B16-GM-CSF	UC San Francisco	N/A
B16-ZsGreen	UC San Francisco	N/A
Experimental Models: Organisms/Strains		
Mouse: C57BL/6J	The Jackson Laboratory	Stock # 000664
Mouse: B6 CD45.1 (B6.SJL-$Ptprc^a$ $Pepc^b$/BoyJ)	The Jackson Laboratory	Stock # 002014
Mouse: OT-II (B6.Cg-Tg(TcraTcrb)425Cbn/J	The Jackson Laboratory	Stock # 004194
Mouse: *Irf4 fl/fl (*B6.129S1-*Irf4tm1Rdf*/J)	The Jackson Laboratory	Stock # 009380
Mouse: *ActB-Cre* (FVB/N-*Tmem163*$^{Tg(ACTB-cre)2Mrt}$/J) received backcrossed to C57/Bl6	The Jackson Laboratory	Stock # 003376
Mouse: *CD11c-Cre* (B6.Cg-Tg(Itgax-cre)1-1Reiz/J)	The Jackson Laboratory	Stock # 008068
Mouse: *Cx3cr1*^{iDTR} (B6N.129P2-*Cx3cr1*$^{tm3(DTR)Litt}$/J)	The Jackson Laboratory	Stock # 025629
Mouse: *Ccr7*−/− (B6.129P2(C)-*Ccr7*^{tm1Rfor}/J)	The Jackson Laboratory	Stock # 006621

(*Continued on next page*)

Continued

REAGENT or RESOURCE	SOURCE	IDENTIFIER
Mouse: *Zbtb46*^{GFP} (B6.129S6(C)-*Zbtb46*$^{tm1.1Kmm}$/J)	The Jackson Laboratory	Stock # 027618
Mouse: *Foxp3*^{DTR} (B6.129(Cg)-*Foxp3*$^{tm3(DTR/GFP)Ayr}$/J)	The Jackson Laboratory	Stock # 016958
Mouse: *Xcr1*^{DTR} (Xcr1$^{tm2(HBEGF/Venus)Ksho}$)	Tsuneyasu Kaisho, Osaka University	MGI: 5544058
Mouse: *Foxp3*$^{Cre/YFP}$ (B6.129(Cg)-*Foxp3*$^{tm4(YFP/icre)Ayr}$/J)	The Jackson Laboratory	Stock # 016959
Mouse: *Itgb8*$^{fl/fl}$ (Itgb8^{tm2Lfr})	Michael Rosenblum, UC San Francisco	MGI: 3608910
Mouse: *Il-10*$^{fl/fl}$ (Il-10 flox)	Susan Kaech, Salk Institute. Generated by Werner Müller.	PMID: 15534372
Mouse: *Areg*−/− (Areg^{tm1Dle})	Marco Conti, UC San Francisco. Generated by David C. Lee.	MGI: 2176531
Deposited Data		
Single cell RNA sequencing data (mouse and human)	This paper	GEO: GSE125680, https://www.ncbi.nlm.nih.gov/gds
Software and Algorithms		
CellRanger 2.0	10X Genomics	10xgenomics.com
STAR	Dobin et al., 2013	code.google.com/p/rna-star/.
Seurat	Satija et al., 2015	https://satijalab.org/seurat/
R: The Project for Statistical Computing	N/A	http://r-project.org

CONTACT FOR REAGENT AND RESOURCE SHARING

Further information and requests for resources and reagents should be directed to and will be fulfilled by the Lead Contact, Matthew F. Krummel (matthew.krummel@ucsf.edu).

EXPERIMENTAL MODEL AND SUBJECT DETAILS

Human Tumor Samples

The human head and neck tumor set consisted of a total of 32 tumors removed from the head and neck region, agnostic to location. The anti-PD-1 responder/non-responder melanoma tumor set was published previously (Barry et al., 2018). All patients consented for tissue collection under a UCSF IRB approved protocol (UCSF IRB# 13-12246 and 14-15342). Samples were obtained after surgical excision with biopsies taken by the Pathology Department to confirm the presence of tumor cells. Patients were selected without regard to prior treatment. Freshly resected samples were placed in ice-cold PBS or Leibovitz's L-15 medium in a 50 mL conical tube and immediately transported to the laboratory for evaluation. Patient samples were coded and flow analysis was scored by separate individuals prior to data agglomeration. All samples were processed and analyzed by flow cytometry, but only those with at least 1,000 live CD45^{+} cell events were included in the analysis.

Mice

All mice were treated in accordance with the regulatory standards of the National Institutes of Health and American Association of Laboratory Animal Care and were approved by the UCSF Institution of Animal Care and Use Committee. The following mice were purchased for acute use or maintained under specific pathogen-free conditions at the University of California, San Francisco Animal Barrier Facility: C57BL/6J, C57BL/6J CD45.1, OT-II, *Irf4*$^{fl/fl}$, *ActB-Cre*, *CD11c*^{Cre}, *Cx3cr1*^{iDTR}, *Ccr7*−/−, *Zbtb46*^{GFP}, *Foxp3*^{DTR}, *Xcr1*^{DTR}, *Foxp3*$^{Cre/YFP}$, *Itgb8*$^{fl/fl}$, *Il-10*$^{fl/fl}$, *Areg*−/−. All mice used in experimentation were bred to a C57BL/6 background. We attempted to use *Irf4*$^{flox/flox}$;*CD11c*^{Cre} but discovered independent breeding cages were producing germline *Irf4* globally deficient pups within a single generation, complicating our findings (data not shown). Mice of either sex ranging in age from 6 – 12 weeks were used for experimentation.

Tumor cell lines

B16-F10 (ATCC, CRL-6475) was purchased. B16-ChOVA (B16^{ChOVA}), a derivative of B16-F10, was created through transduction of B16-F10 with an mCherry-OVA (ChOVA) fusion construct identical to that used in previous studies in our lab (Roberts et al., 2016). B78^{ChOVA}, derived from the parental B78 subline of B16, was generated in our laboratory and described previously (Broz et al., 2014). B16-ZsGreen (B16^{ZsGr}) was previously generated in our laboratory as described (Headley et al., 2016). B16$^{GM\text{-}CSF}$ (GVAX) (Dranoff et al., 1993) were acquired from the laboratory of Dr. Lawrence Fong at UC San Francisco. Adherent cell lines were cultured at 37°C in 5% CO_2 in DMEM (Invitrogen), 10% FCS (Benchmark), Pen/Strep/Glut (Invitrogen).

METHOD DETAILS

Tumor cell injections and tumor growth experiments

For tumor cell injection, adherent tumor cells were lifted using 0.05% Trypsin-EDTA (Thermo Fisher Scientific) and washed 3X with DPBS (Thermo Fisher Scientific). $1.0x10^5$ – $2.5x10^5$ tumor cells were resuspended in DPBS and mixed 1:1 with Matrigel GFR (Corning) for a final injection volume of 50 μL. Mice anesthetized with isoflurane (Henry Schein) were shaved on their flank and injected subcutaneously either unilaterally or bilaterally depending on the experimental setup.

For tumor measurements, tumors were typically measured 3 times per week using electronic calipers. Tumor volume was calculated through the formula $V = 0.5(w^2 \times l)$. Mice were removed from the study and euthanized when tumors exceeded a volume of 1000 mm^3.

Single Cell RNA Sequencing (scRNA-Seq)

For mouse scRNA-seq, live $CD90.2^-$ $B220^-$ $Ly6G^-$ $NK1.1^-CD11b^+$ and/or $CD11c^+$ cells were sorted from inguinal and axillary LN with a BD FACSAria Fusion. For human scRNA-seq, live $CD3^-CD19/20^-CD56^-$ cells were sorted from a melanoma-draining LN on a BD FACSAria Fusion. After sorting, cells were pelleted and resuspended at $1x10^3$ cells/μl in 0.04%BSA/PBA and loaded onto the Chromium Controller (10X Genomics). Samples were processed for single-cell encapsulation and cDNA library generation using the Chromium Single Cell 3′ v2 Reagent Kits (10X Genomics). The library was subsequently sequenced on an Illumina HiSeq 4000 (Illumina).

Single Cell Data Processing

Sequencing data was processed using 10X Genomics Cell Ranger V1.2 pipeline. The Cell Ranger subroutine *mkfastq* converted raw, Illumina bcl files to fastqs which were then passed to Cell Ranger's *count,* which aligned all reads using the aligner STAR (Dobin et al., 2013) against UCSC mm10 or GRCh38 genomes for mouse and human cells, respectively. After filtering reads with redundant unique molecular identifiers (UMI), *count* generated a final gene-cellular barcode matrix. Both *mkfastq* and *count* were run with default parameters.

Cellular Identification and Clustering

For each sample, the gene - barcode matrix was passed to the R (v. 3.4.3) software package Seurat (Satija et al., 2015) (https://satijalab.org/seurat) (v2.3.0) for all downstream analyses. We then filtered on cells that expressed a minimum of 200 genes and required that all genes be expressed in at least 3 cells. We also removed cells that contained > 5% reads associated with cell cycle genes (Kowalczyk et al., 2015; Macosko et al., 2015). Count data was then log2 transformed and scaled using each cell's proportion of cell cycle genes as a nuisance factor (implemented in Seurat's *ScaleData* function) to correct for any remaining cell cycle effect in downstream clustering and differential expression analyses. For each sample, principal component (PC) analysis was performed on a set of highly variable genes defined by Seurat's *FindVariableGenes* function. Genes associated with the resulting PCs (chosen by visual inspection of scree plots) were then used for graph-based cluster identification and subsequent dimensionality reduction using t-distributed stochastic neighbor embedding (tSNE). Cluster-based marker identification and differential expression were performed using Seurat's *FindAllMarkers* for all between-cluster comparisons.

ImmGen Signature Generation

To generate *a priori* signatures for the myeloid cell types that we expected to find in the mouse tdLN sample, we downloaded microarray based transcriptional profiles from the Immunological Genome Project data Phase 1(Heng and Painter, 2008) (GEO: GSE15907). See Table S1 for the specific samples used.

For each ImmGen population, we performed DE analysis comparing samples from the population of interest to the aggregate of the remaining 6 groups using the R package *limma* (Ritchie et al., 2015). We ordered the top 20 genes with the smallest FDR values (Benjamini and Hochberg, 1995) by fold change (excluding any genes that were downregulated in the group of interest) and then cross referenced the resulting list with the single cell expression matrix from each sample. This left genes that were both highly differentially expressed in the IMMGEN profiles and expressed in our single cell datasets of interest. The top 10 genes (or fewer if less than 10 genes remained) by fold change were then median normalized and aggregated to create a single "signature gene" for each cell type. These signature genes were 0-1 scaled and plotted in the context of the *t*-SNE dimensionality reduction to show cellular location.

Sequencing Sample Aggregation

In order to generate pairwise aggregations between samples and control for potential batch effects, we used Seurat's Canonical Correlation Analysis (CCA) functionality. All post-filtered cells from each of the single sample analyses were used in the aggregate. CCA was performed on the union of the 2000 genes with highest dispersions from each dataset. The number of canonical correlation vectors (CCVs) used in downstream clustering and *t*-SNE analyses was chosen by visual inspection of heatmaps of genes associated with those top CCVs. Results were robust to moderate changes in this final number of CCVs.

Mouse Tissue Digestion and Flow Staining

Tumor and LN tissues were harvested and enzymatically digested with 0.2 mg/ml DNase I (Sigma-Aldrich), 100 U/ml Collagenase I (Worthington Biochemical), and 500 U/ml Collagenase Type IV (Worthington Biochemical) for 30-45 minutes at 37°C. TdLN included inguinal and axillary LN. Tumor samples were subjected to consistent agitation during this time and LN samples were rapidly pipetted at the half-point time. Samples were filtered to generate a single-cell suspension and washed with stain media (PBS, 2% FCS). For bone marrow cells, mouse femurs and tibias were flushed with stain media and subsequently underwent red blood cell lysis.

Cells harvested from these tissues or *in vitro* culture were washed with PBS and stained with Zombie NIR fixable viability dye (BioLegend) for 30 minutes at 4°C to distinguish live and dead cells. Cells were then washed with stain media and non-specific binding was blocked with anti-CD16/32 (BioXCell), and 2% rat serum (Invitrogen) and 2% Armenian hamster serum (Innovative Research). Cell surface proteins were then stained on ice for 30 minutes. Cells were washed again and re-suspended with stain media prior to collection and analysis on a BD Fortesssa or LSR-II flow cytometer. When applicable, black latex beads were added to the sample for quantification of absolute cell number. For intracellular stains, cells were fixed and permeabilized with the FoxP3/Transcription Factor Staining Buffer Set (Thermo Fisher Scientific) after surface marker staining. Intracellular antibodies were stained in permeabilization buffer with 2% rat serum for at least 30 minutes at room temperature.

Human Tissue Digestion and Flow Staining

Tumor or LN tissue was thoroughly chopped with surgical scissors and transferred to GentleMACs C Tubes (Miltenyi Biotec) containing 20 uL/mL Liberase TL (5 mg/ml, Roche) and 50 U/ml DNase I (Roche) in RPMI 1640 per 0.3 g tissue. GentleMACs C Tubes were then installed onto the GentleMACs Octo Dissociator (Miltenyi Biotec) and incubated according to the manufacturer's instructions. Samples were then quenched with 10 mL of sort buffer (PBS/2% FCS/2mM EDTA), filtered through 100 um filters and spun down. Red blood cell lysis was performed with 175 mM ammonium chloride.

Cells were then incubated with Human FcX (Biolegend) to prevent non-specific antibody binding. Cells were then washed in DPBS and incubated with Zombie Aqua Fixable Viability Dye (Biolegend). Following viability dye, cells were washed with sort buffer and incubated with cell surface antibodies for 30 minutes on ice and subsequently fixed in either Fixation Buffer (BD Biosciences) or in Foxp3/Transcription Factor Staining Buffer Set (ThermoFisher Scientific) if intracellular staining was required.

APC-T cell *In Vitro* Co-Culture Assays

APC populations were double-sorted (yield followed by purity) from tdLN using a BD FACSAria Fusion and co-cultured with $2x10^4$ isolated eFluor670-labeled OT-II T cells at a 1:5 ratio in complete RPMI (Pen/Strep, NEAA, NaPyr, 2-ME, 10% FCS) in 96-well V-bottom plates. Cells were harvested for analysis 3 days later. OVA peptide 323-339 (GenScript) was added to wells at 1 μg/ml as a positive control.

Mouse T cell Isolation and *In Vivo* Adoptive T Cell Transfer

Inguinal, axillary, brachial, superficial cervical and mesenteric LN were isolated from CD45.1$^+$ OT-II mice. LN were smashed through 100 um filters and subsequently spun down and counted. CD4$^+$ T cells were then isolated using EasySep CD4 negative-selection kits (STEMCELL Technologies).

$1x10^5$ isolated CD45.1$^+$ CD4$^+$ OT-II T cells were either transferred immediately in cases of PMA/Ionomycin restimulation experiments or labeled with Cell Proliferation Dye eFluor670 (Thermo Fisher Scientific) and $1.0\text{-}5.0x10^5$ cells were adoptively transferred to CD45.2$^+$ mice. LN were harvested for proliferation analysis at day 3 post-transfer and for PMA/ionomycin re-stimulation at day 7 post-transfer. *XCR1*^{DTR} and *Cx3cr1*^{iDTR} mice were treated with 500 ng of DT every other day beginning the day prior to OT-II transfer through the experimental end point. *Foxp3*^{DTR} mice were injected with DT for two days prior to OT-II transfer and then the day following OT-II transfer.

T Cell Cytokine Analysis

For cytokine analysis of endogenous or adoptively transferred T cells, cells from either LN or tumors were used for re-stimulation. Single cell suspensions were incubated with 50 ng/ml PMA (Sigma-Aldrich), 500 ng/ml ionomycin (Thermo Fisher Scientific), 3 μg/ml brefeldin A (Cayman Chemical Company), and 2 μM monensin (Thermo Fisher Scientific) for 5-6 hours in complete RPMI and stained for surface and intracellular proteins using the Foxp3/Transcription Factor Staining Buffer Set (ThermoFisher Scientific).

In Vivo Treatments

For diphtheria toxin (DT), while treatment schedules varied depending upon mouse genetic strain or type of experiment, mice received 500 ng boluses of un-nicked DT (List Biologics, 150) intraperitoneally. *Foxp3*^{DTR}, *XCR1*^{DTR} and *Cx3cr1*^{iDTR} mice were typically injected on days 9, 10 and 12 followed by flow cytometric analysis at day 14.

For comparisons of CD4$^+$ T_{conv} priming between steady-state, tumor-bearing and influenza-infected conditions, mice were injected subcutaneously with either 20 μg of endotoxin-free ovalbumin (Invivogen) in 50 μL of PBS or $2.0x10^5$ B16^{ChOVA}. Mice receiving influenza were infected intranasally with $1x10^5$ PFU of X31-OT-II (Thomas et al., 2006), prepared as previously described (GeurtsvanKessel et al., 2008).CD45.1$^+$ OT-II$^+$ CD4$^+$ T cells were transferred intravenously 2 days after ovalbumin and X31-OT-II treatment and 14 days after B16^{ChOVA} injection.

To assess CD4/CD8 T cell dependency for tumor rejection following T_{reg} depletion or GVAX/anti-CTLA-4 treatment, mice were injected with 250 μg of isotype (Clone: LTF-2, BioXCell), anti-CD4 (Clone: GK1.5, BioXCell) or anti-CD8a (Clone: 2.43, BioXCell) was injected intraperitoneally at days 10, 13 and 16 post-tumor injection for *Foxp3*^{DTR} and days 4, 7 and 10 for GVAX/anti-CTLA-4 treatment.

To assess the requirement of T cell LN egress, control or *Foxp3*^{DTR} mice were treated intraperitoneally with 500 ng of DT on days 9, 10 and 12 post-tumor injection and with 200 μg FTY720 (Cayman Chemicals) every day beginning on day 8 post-tumor injection through the end of the experiment.

For Fc-modified anti-CTLA-4 experiments, mice were injected with $2x10^5$ B16^{ZsGreen} cells. On days 7, 9, 10, 11 and 13 post-tumor injection, mice received 250 μg of mouse IgG2c isotype, anti-CTLA-4 IgG2c (modified clone 9D9, Bristol-Myers-Squibb), mouse IgG1 isotype or anti-CTLA-4 IgG1 (modified clone 9D9, Bristol-Myers-Squibb) intraperitoneally.

For GVAX/anti-CTLA-4 experiments, mice were injected with either $1x10^5$ (tumor growth) or $2x10^5$ B16-F10 (cellular analysis). On days 3, 6 and 9 post-tumor injection, mice were injected subcutaneously on their contralateral flank with either PBS or $1x10^6$ 50 Gy-irradiated GVAX cells and received either 250 μg anti-CTLA-4 (9H10, BioXCell) or Syrian hamster IgG isotype (BioXcell) intraperitoneally on day 3, and 100 μg of antibody on days 6 and 9.

QUANTIFICATION AND STATISTICAL ANALYSIS

Statistical analysis

Unless specifically noted, data displayed is from a representative experiment of $\geq$ 2 independent experiments. Experimental group assignment was determined by genotype or, if all wild-type mice, by random designation. Error bars represent mean ± SEM calculated using Prism unless otherwise noted. Statistical analyses were performed using GraphPad Prism software. For pairwise comparisons, unpaired t tests were used unless otherwise noted. For statistical measures between more than two groups, one-way ANOVA would be performed unless otherwise noted. Comparisons found to be nonsignificant are not shown. Investigators were not blinded to group assignment during experimental procedures or analysis.

DATA AND SOFTWARE AVAILABILITY

Data Resources

The accession number for the expression matrix for the single-cell RNA-sequencing reported in this paper is GEO: GSE125680.

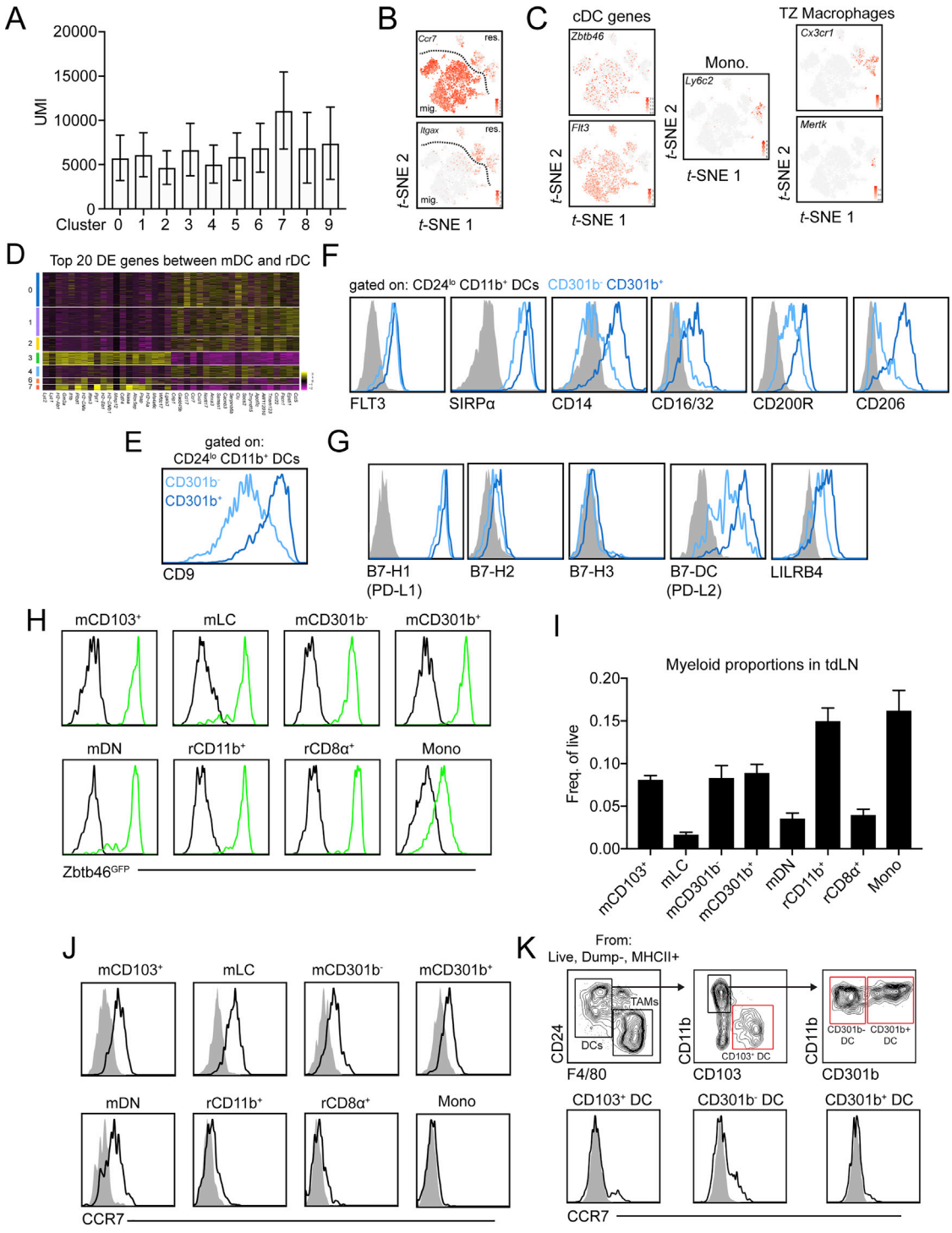

Figure S1. Unbiased scRNA-Seq of Myeloid Cells in the tdLN Reveals Extensive Heterogeneity, Related to Figure 1

(A) Average cell UMI across the 10 clusters present in the tdLN *t*-SNE (Figure 1A) with bars denoting standard deviation.

(B) Gene expression overlay of *Ccr7* and *Itgax* plotted on the tdLN *t*-SNE. Scale bar indicates relative expression level.

(C) Gene expression overlay of canonical cDC markers, *Zbtb46* and *Flt3* on the tdLN *t*-SNE (left), monocyte marker *Ly6c2* (middle) and T cell zone macrophage markers *Cx3cr1* and *Mertk* (right).

(D) Heatmap displaying top 20 DE genes for mDC and rDC when clusters 0, 1, 2, 4 and 6 are compared to clusters 3 and 7 (ranked by log N fold change).

(E) Surface expression of CD9 on CD301b$^-$ and CD301b$^+$ CD11b$^+$ CD24^{lo} DC populations.

(F) Surface expression of denoted cell markers on mCD301b$^-$ and mCD301b$^+$.

(legend continued on next page)

(G) Surface expression of known inhibitory receptors on mCD301b$^-$ and mCD301b$^+$.
(H) GFP expression in myeloid populations detected in tdLNs from tumor-bearing *Zbtb46*^{GFP} (green) and control (black) mice.
(I) Frequency of myeloid populations within the tdLN.
(J) Surface levels of CCR7 on tdLN myeloid populations.
(K) Gating strategy of myeloid populations in mouse TME (top) and surface expression of CCR7 on tumor DC populations (bottom).

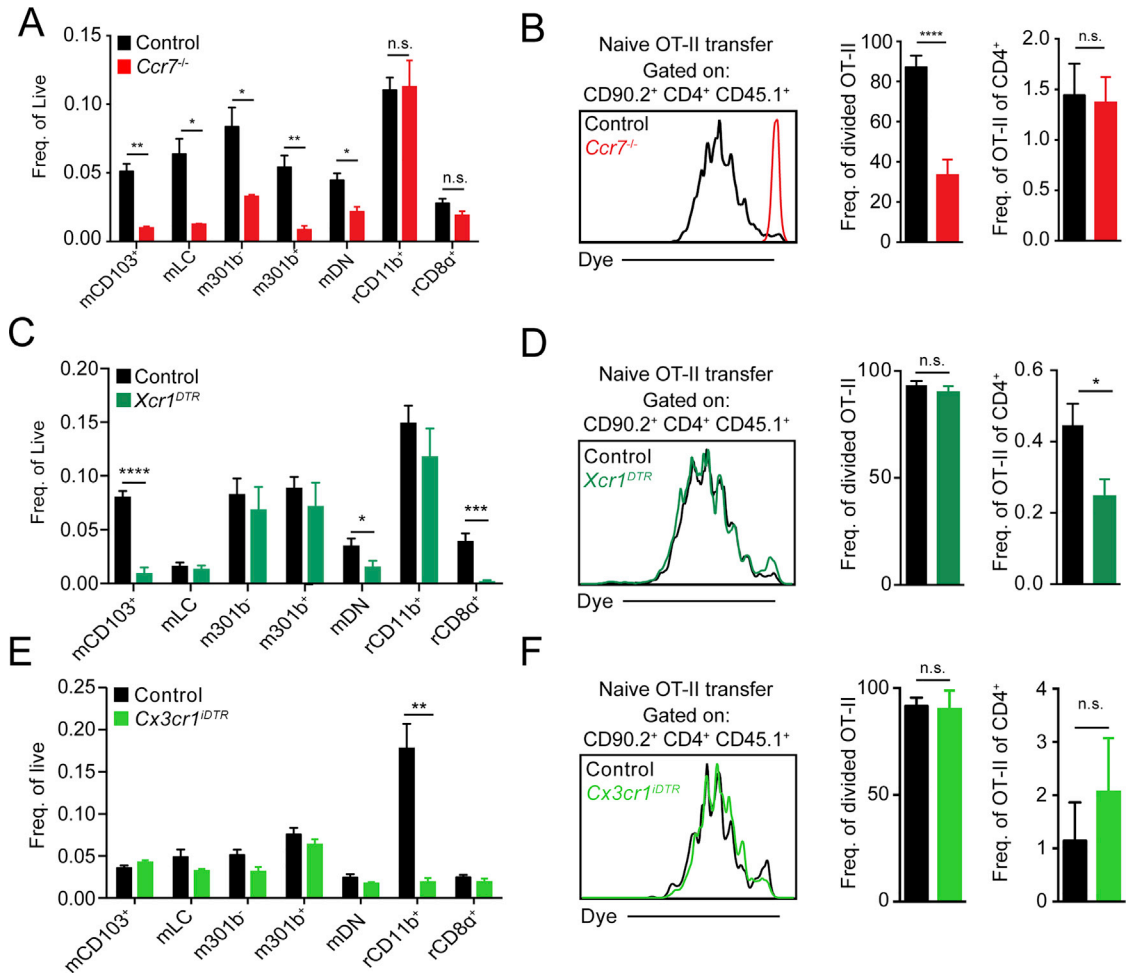

Figure S2. mCD301b$^{-/+}$ cDC2 Are Uniquely Able to Induce Anti-tumor CD4$^+$ T$_{conv}$ Proliferation but Fail to Initiate CD4$^+$ T$_{conv}$ Differentiation, Related to Figure 2

(A) Frequency of tdLN DC populations in control or *Ccr7*$^{-/-}$ tumor-bearing mice.

(B) Proliferation of CD45.1$^+$ CD4$^+$ OT-II T cells in tdLN that had been transferred to control or *Ccr7*$^{-/-}$ tumor-bearing mice 3 days prior as assessed by dye dilution (left), the frequency that had divided (middle), and their frequency of endogenous CD4$^+$ T cells (right).

(C) Frequency of tdLN DC populations in control or *Xcr1*^{DTR} tumor-bearing mice.

(D) Proliferation of transferred CD45.1$^+$ CD4$^+$ OT-II T cells in tdLN of control or *Xcr1*^{DTR} tumor-bearing mice with analysis of dye dilution (left), the frequency that had divided (middle), and their frequency of endogenous CD4$^+$ T cells (right) 3 days post-transfer.

(E) Frequency of tdLN DC populations in control or *Cx3cr1*^{iDTR} tumor-bearing mice.

(F) Proliferation of transferred CD45.1$^+$ CD4$^+$ OT-II T cells in tdLN of control or *Cx3cr1*^{iDTR} tumor-bearing mice with analysis of dye dilution (left), the frequency that had divided (middle), and their frequency of endogenous CD4$^+$ T cells (right) 3 days post-transfer.

Data are represented as average ± SEM unless explicitly specified. *p < 0.05, **p < 0.01, ***p < 0.001, ****p < 0.0001.

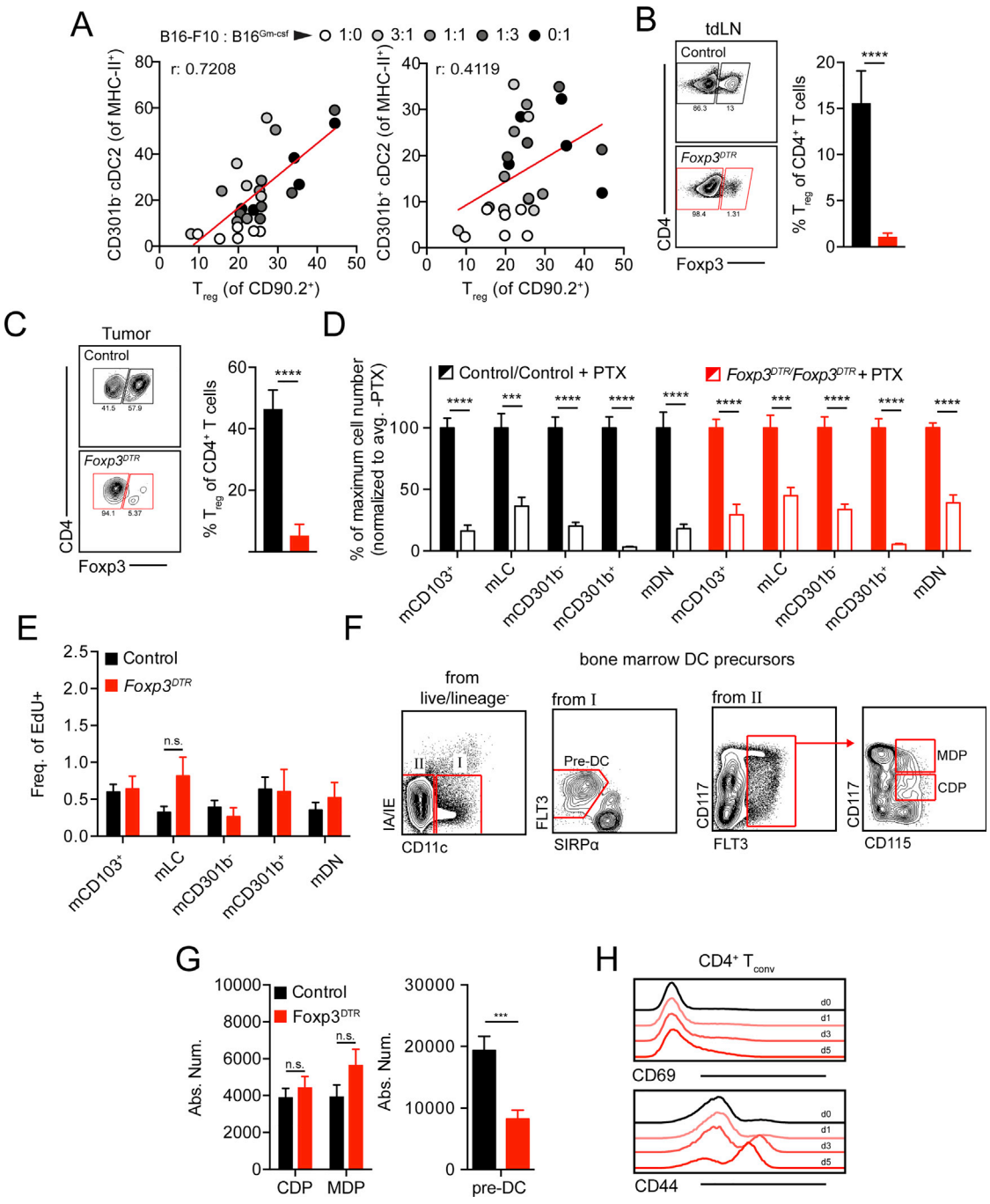

Figure S3. T_{reg} Depletion Enhances cDC2 Migration to the tdLN and Unleashes an Anti-tumor $CD4^+$ T_{conv} Response, Related to Figure 3

(A) Dot plot correlation of intratumoral $CD11b^+$ $CD301b^-$ cDC2 frequency within MHC-II^+ cells (left) or $CD11b^+$ $CD301b^-$ cDC2 within MHC-II^+ (right) and T_{reg} frequency within $CD90.2^+$ T cells. Best fit line shown. Pearson correlation performed for r value. Data pooled from two experiments.

(B and C) Gating example of FoxP3 expression in $CD4^+$ T cells of DT-treated control and *Foxp3*^{DTR} mice and the frequency of $FoxP3^+$ T_{reg} within $CD4^+$ T cells in the (B) tdLN or (C) tumor.

(D) Control and *Foxp3*^{DTR} B16-F10 tumor-bearing mice were treated with DT and PTX and absolute number of migratory DC in the tdLN were analyzed at day 5 post-DT. Samples normalized to their genetic PTX-untreated condition. Representative data of two independent experiments displayed.

(E) Frequency of EdU incorporation after 2 h within migratory DC from tumor-bearing control and *Foxp3*^{DTR} mice 2 days post-DT administration.

(F) Representative gating scheme for DC precursors in mouse bone marrow.

(G) Absolute numbers of DC precursors in bone marrow of tumor-bearing control and Foxp3DTR animals 5 days after DT administration.

(H) Representative histograms of CD69 and CD44 surface levels from data in Figure 3H.

Data are represented as ± SEM. *p < 0.05, **p < 0.01, ***p < 0.001, ****p < 0.0001.

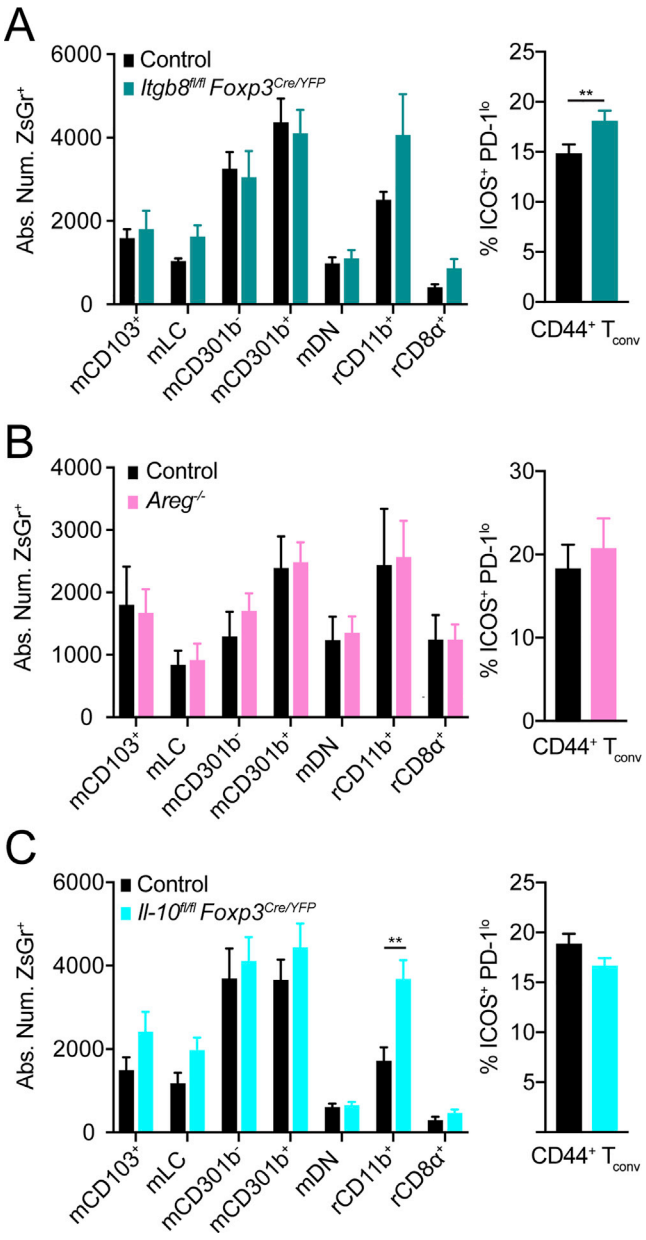

Figure S4. Canonical T_{reg} Suppressive Cytokines Do Not Impact cDC2 Migration nor Antitumor $CD4^+$ T_{conv} Quality, Related to Figures 3 and 4

(A) Analysis of immune populations in tdLN from $B16^{ZsGreen}$ tumor-bearing control and *Itgb8*$^{fl/fl}$*Foxp3*^{CreYFP} mice. Absolute number of $ZsGreen^+$ DC populations (left) and frequency of $CD44^+$ $CD4^+$ T_{conv} with $ICOS^+$ $PD\text{-}1^{lo}$ surface phenotype (right).

(B) Analysis of immune populations in tdLN from $B16^{ZsGreen}$ tumor-bearing control and *Areg*−/− mice. Absolute number of $ZsGreen^+$ DC populations (left) and frequency of $CD44^+$ $CD4^+$ T_{conv} with $ICOS^+$ $PD\text{-}1^{lo}$ surface phenotype (right).

(C) Analysis of immune populations in tdLN from $B16^{ZsGreen}$ tumor-bearing control and *Il-10*$^{fl/fl}$*Foxp3*^{CreYFP} mice. Absolute number of $ZsGreen^+$ DC populations (left) and frequency of $CD44^+$ $CD4^+$ T_{conv} with $ICOS^+$ $PD\text{-}1^{lo}$ surface phenotype (right).

Data are represented as average ± SEM unless explicitly specified. *p < 0.05, **p < 0.01, ***p < 0.001, ****p < 0.0001.

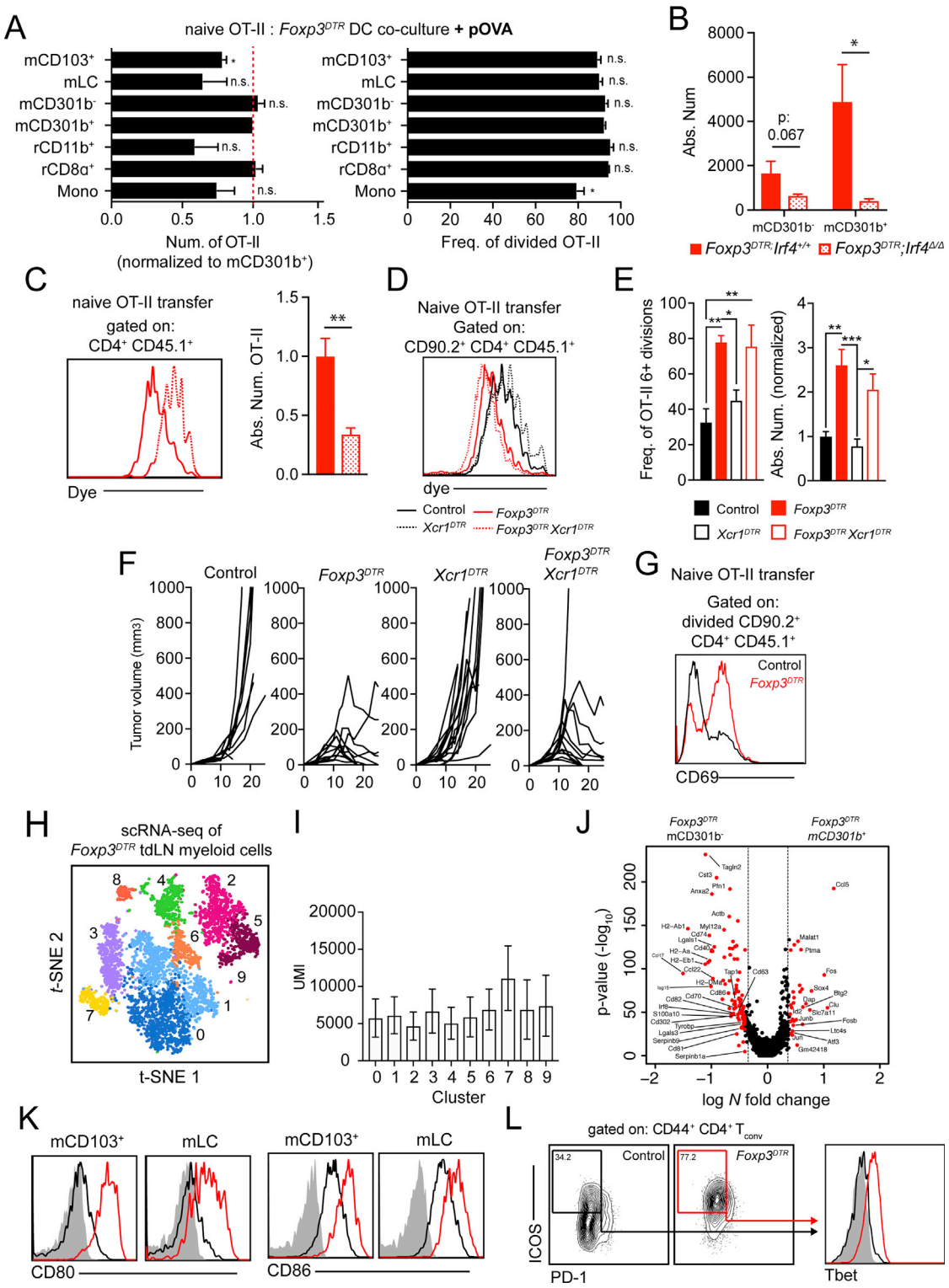

Figure S5. T_{reg} Depletion Enhances cDC2 Function and CD4$^+$ T_{conv} Differentiation, Related to Figure 4

(A) OT-II T cells were co-cultured with APC populations sorted from *Foxp3*^{DTR} tdLN in media containing exogenous OVA peptide (323-339) and analyzed 3 days later for the absolute number of live (left) OT-II T cells recovered and the frequency of cells that had divided (right). Data were normalized and statistically compared to mCD301b$^+$ condition.

(B) Analysis of CD11b$^+$ cDC2 immune populations in tdLN from B16^{ChOVA} tumor-bearing *Foxp3*^{DTR} *Irf4*$^{+/+}$ and *Foxp3*^{DTR} *Irf4*$^{\Delta/\Delta}$ mice.

(legend continued on next page)

(C) Proliferation of CD45.1$^+$ OT-II T cells in tdLN that had been transferred to *Foxp3^{DTR}Irf4$^{+/+}$ Foxp3^{DTR}Irf4$^{\Delta/\Delta}$* mice 3 days prior as assessed by dye dilution (left) and absolute number (right). (B,C) was a preliminary experiment that was only performed once.
(D) Proliferation of CD45.1$^+$ OT-II T cells in tdLN that had been transferred to control, *Foxp3^{DTR}*, *Xcr1*^{DTR}, or *Foxp3^{DTR}Xcr1*^{DTR} tumor-bearing mice 3 days prior as assessed by dye dilution.
(E) Frequency of OT-II that divided 6+ times (left). The absolute number of transferred OT-II (right).
(F) Tumor growth from control, *Foxp3*^{DTR}*, Xcr1*^{DTR} *and Foxp3*^{DTR}*Xcr1*^{DTR} mice. Results depict tumor growth curves of individual mice.
(G) Cell surface CD69 levels on divided OT-II T cells 3 days after transfer into control and *Foxp3^{DTR}* B16^{ChOVA} tumor-bearing mice. Representative data of three independent experiments displayed.
(H) *t*-SNE plot and graph-based clustering of CD90.2$^-$ B220$^-$ NK1.1$^-$ CD11b$^+$ and/or CD11c$^+$ myeloid cells sorted from a DT-treated *Foxp3^{DTR}* B16F10 tdLN and processed for scRNA-seq. Each dot represents a single cell.
(I) Average cell UMI across the 10 clusters present in the primary *Foxp3^{DTR}* tdLN *t*-SNE from Figure S5H with bars denoting standard deviation.
(J) Volcano plots displaying DE genes comparing *Foxp3^{DTR}* tdLN mCD301b$^-$ and mCD301b$^+$. Log *N* fold cutoff of 0.4 used. Genes of interest labeled.
(K) Cell surface levels of CD80 (left) and CD86 (right) on mCD103$^+$, mLC, in control and *Foxp3^{DTR}* tdLN.
(L) Representative flow cytometry plots of ICOS, PD-1 and T-bet expression in CD44$^+$ CD4$^+$ T_{conv} within the tdLN of control and *Foxp3^{DTR}* mice.
Data are represented as average ± SEM unless explicitly specified. *p < 0.05, **p < 0.01, ***p < 0.001, ****p < 0.0001.

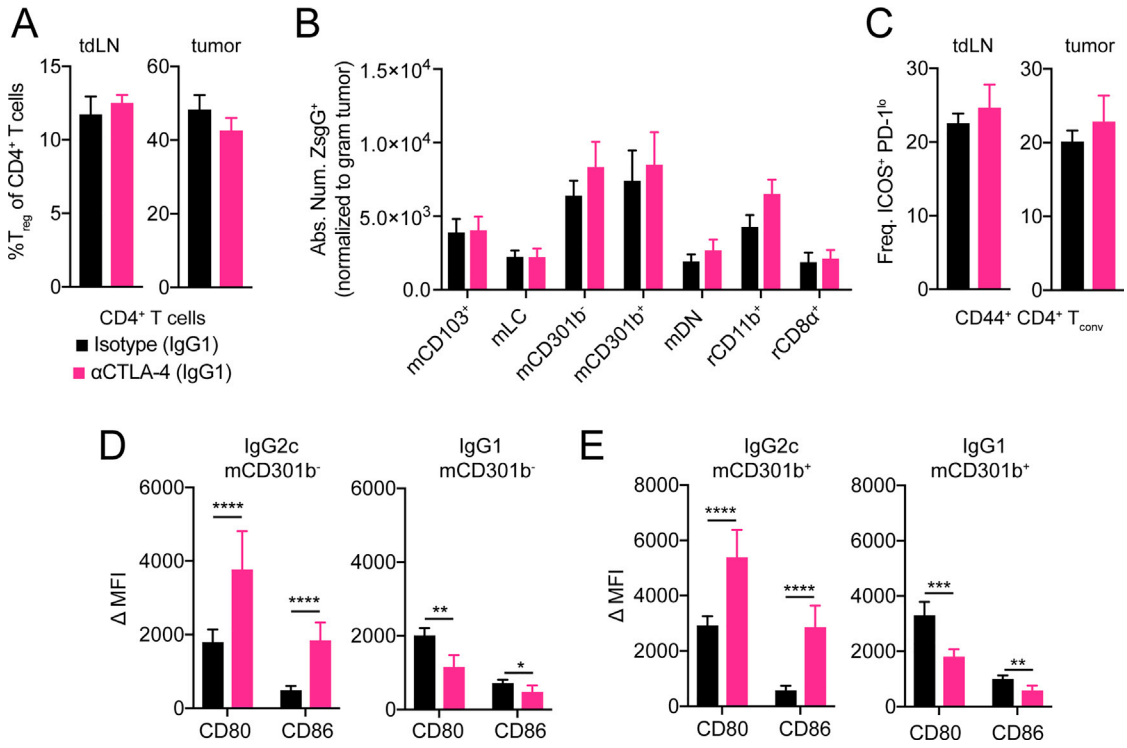

Figure S6. Anti-CTLA-4 Induces Expansion and Functional Enhancement of CD11b$^+$ cDC2, Related to Figure 5

(A) Frequency of T_{reg} within CD4$^+$ T cells in tdLN (left) or tumor (right) from B16^{ZsGreen} tumor-bearing mice treated with mouse IgG1 isotype or anti-CTLA-4 (mouse IgG1).

(B) Absolute number of ZsGreen$^+$ DC in tdLN (normalized to weight of associated tumor).

(C) Frequency of CD44$^+$ CD4$^+$ T_{conv} with ICOS$^+$ PD-1^{lo} surface phenotype in tdLN (left) or tumor (right).

(D) ΔMFI (CD80/CD86 MFI – Isotype MFI) from mCD301b$^-$ from tdLN of B16^{ZsGreen} tumor-bearing mice treated with either Isotype/anti-CTLA-4 (mouse IgG2c) (left) or Isotype/anti-CTLA-4 (mouse IgG1) (right).

(E) ΔMFI (CD80/CD86 MFI – Isotype MFI) from mCD301b$^+$ from tdLN of B16^{ZsGreen} tumor-bearing mice treated with either Isotype/anti-CTLA-4 (mouse IgG2c) (left) or Isotype/anti-CTLA-4 (mouse IgG1) (right).

Data are represented as average ± SEM unless explicitly specified. *p < 0.05, **p < 0.01, ***p < 0.001, ****p < 0.0001.

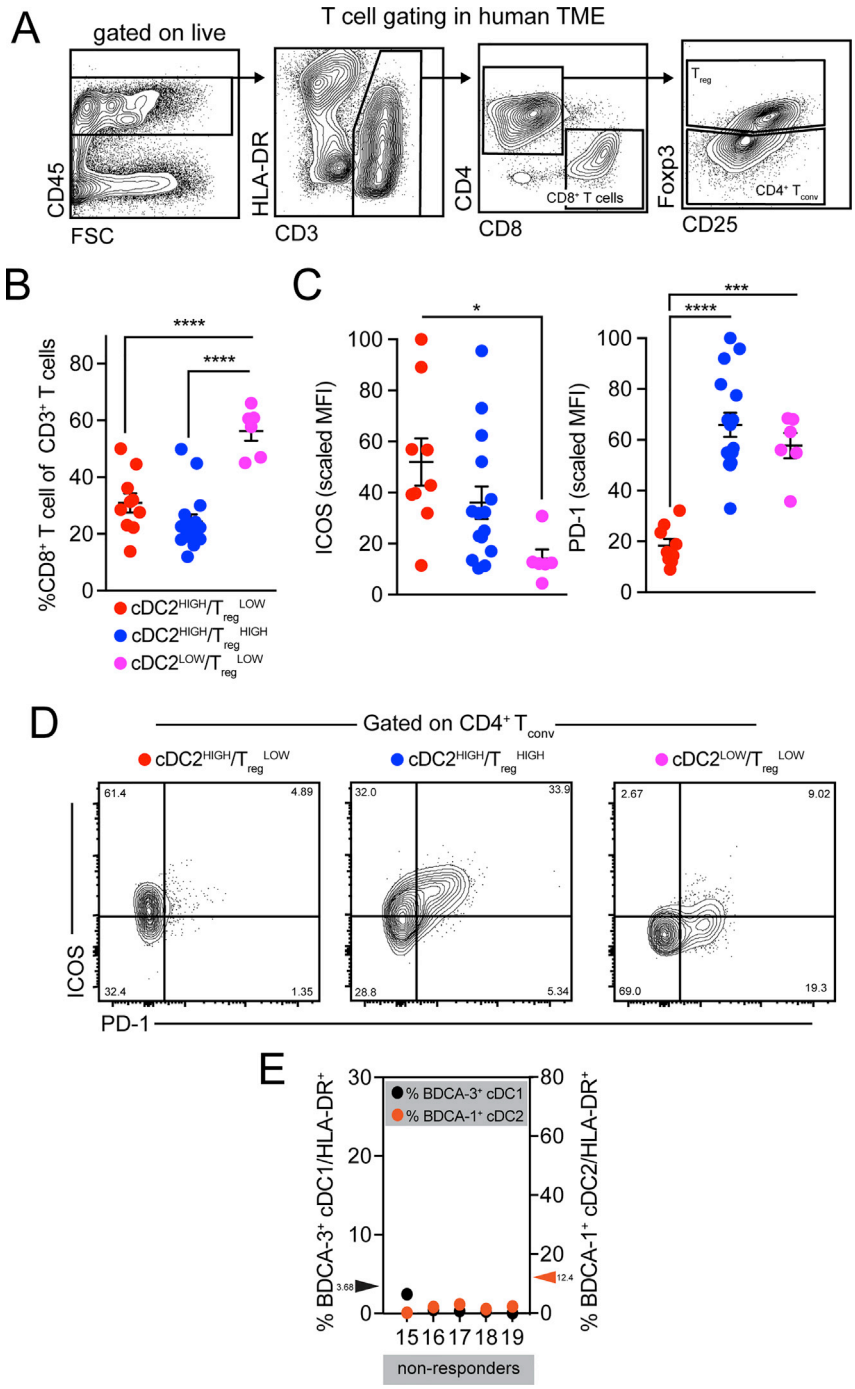

Figure S7. BDCA-1$^+$ cDC2 Proportion in Human TME Impacts CD4$^+$ T$_{conv}$ Proportion and Quality, Related to Figure 7

(A) Gating strategy of human HNSC TME to identify T cell populations.

(B) Frequency of CD8$^+$ T cells (of CD3$^+$ T cells) within each type of HNSC TME identified in Figure 7A.

(C) Scaled ICOS (left) and PD-1 (right) MFI on CD4$^+$ T$_{conv}$ within each type of HNSC TME identified in Figure 7A (left).

(D) Representative example of ICOS and PD-1 expression on CD4$^+$ T$_{conv}$ within each HNSC TME subset.

(E) Frequency of BDCA-3$^+$ cDC1 (black) and BDCA-1+ cDC2 (orange) within HLA-DR$^+$ cells in human melanoma tumors from 5 anti-PD-1 non-responders.

Data are represented as average ± SEM unless explicitly specified. *p < 0.05, **p < 0.01, ***p < 0.001, ****p < 0.0001.